UNIVERSIDADE FEDERAL DE SÃO CARLOS
CENTRO DE CIÊNCIAS EXATAS E DE TECNOLOGIA
DEPARTAMENTO DE QUÍMICA
PROGRAMA DE PÓS-GRADUAÇÃO EM QUÍMICA
UNIVERSITAT JAUME I
DEPARTAMENT DE QUÍMICA FÍSICA I ANALÍTICA
PROGRAMA DE DOCTORADO EN CIENCIAS

UNRAVELING THE MECHANISM OF CH_3CH_2OH DEHYDROGENATION ON m-ZrO_2(111) SURFACE, Au_{13} CLUSTER, AND Au_{13} CLUSTER/m-ZrO_2(111) SURFACE: A DFT AND MICROKINETIC MODELING STUDY

Leonardo Henrique de Morais*

Thesis presented as part of the
requirements for obtaining the title of
DOCTOR OF SCIENCE, concentration
area: PHYSICAL CHEMISTRY.

Advisor UFSCar: Alejandro López-Castillo
Advisor UJI: Juan Andrés
Co-advisor UJI: Amanda Fernandes Gouveia

* Scholarship holder from the Coordination for the Improvement of Higher Education Personnel Foundation (CAPES): grants nº 88887.500150/2020-00 and Institutional Internationalization Program (CAPES-PrInt) nº 88887.836086/2023-00.

São Carlos - SP
2024

UNIVERSIDADE FEDERAL DE SÃO CARLOS

Centro de Ciências Exatas e de Tecnologia
Programa de Pós-Graduação em Química

Folha de Aprovação

Defesa de Tese de Doutorado do candidato Leonardo Henrique de Morais, realizada em 16/12/2024.

Comissão Julgadora:

Prof. Dr. Alejandro Lopez Castillo (UFSCar)

Profa. Dra. Lourdes Gracia Edo (UV)

Prof. Dr. Miguel Ángel San-Miguel Barrera (UNICAMP)

Prof. Dr. Gabriel Luiz Cruz de Souza (UFSCar)

Prof. Dr. Luis Antonio Cabral (UNESP)

O Relatório de Defesa assinado pelos membros da Comissão Julgadora encontra-se arquivado junto ao Programa de Pós-Graduação em Química.

I dedicate this work to my family and friends for all their support, understanding and contribution.

Acknowledgments

First and foremost, I thank God, who guides, protects, and watches over me in both good and difficult times. He has never abandoned me and has always given me the strength to carry on. In moments of joy, it is to Him that I have expressed my gratitude in prayer, as He listens, answers, and strengthens my faith.

To my parents, I am deeply grateful for their immense love, care, and support throughout this journey. They have always believed in me and stood by my side, teaching me to never forget where I come from, to never harm others, and to always strive for professional growth.

To my sister, Juliana, who during my doctoral studies moved to a new place and met someone who completes her, my new brother-in-law Kevin. Although we haven’t spent much time together, he has always been a pleasant and kind presence.

To the woman who made São Carlos my comfort zone and whom I now call my wife, Rosana. Not only did I gain her love, but I was also welcomed into an incredible family—Rita, Miriam, Sr. Luiz, and Ms. Maryhelena—who make our weekends even more enjoyable.

I would like to thank Professor Alejandro for his guidance and collaboration over the years. I am also thankful to Professor Juan Andrés and Amanda Fernandes Gouveia for their support and the knowledge I have gained along this path.

To my colleagues and friends from my international experiences at Universitat Jaume I (UJI), Ruhr-Universität Bochum (RUB), and the CHITEL conference.

Lastly, I am grateful to CAPES for financially supporting me (grants 88887.500150/2020-00 and 88887.836086/2023-00), Universitat Jaume I (project UJI-B2022–56), Generalitat Valenciana (Conselleria de Innovación, Universidades, Ciencia y Sociedad Digital – project CIAICO/2021/122, and

Ministerio de Ciencia e Innovación de España (project PID2022–141089NB-I00) for financially supporting this research.

List of Tables

List of Figures

Resumo

DESVENDANDO O MECANISMO DE DESIDROGENAÇÃO DO CH_3CH_2OH NA SUPERFÍCIE m-ZrO_2(111), CLUSTER DE Au_{13} E SUPERFÍCIE DO CLUSTER Au_{13}/m-ZrO_2(111): UM ESTUDO DE MODELAGEM DFT E MICROCINÉTICA. Neste estudo, investigamos a desidrogenação do etanol e a produção de CH_3CHO e H_2 na superfície de m-ZrO_2(111), um cluster de Au_{13} e a superfície de Au_{13}/m-ZrO_2(111), usando simulações da teoria do funcional da densidade. Nosso principal objetivo é elucidar os mecanismos de reação por meio da análise termodinâmica e cinética desses processos catalíticos, identificando os estados de transição. Para dar mais validade a essas descobertas, empregamos um modelo microcinético para calcular as constantes de taxa, obtendo uma compreensão detalhada e abrangente das vias de reação envolvidas. Os cálculos de primeiros princípios foram realizados usando o pacote Quantum ESPRESSO, aplicando o funcional BEEF-vdW para interações de troca e correlação. O sistema modelo foi construído em uma supercélula bidimensional com condições de limite periódicas nas direções x e y, enquanto uma camada de vácuo de 15 Å foi introduzida ao longo da direção z para evitar interações entre as supercélulas periódicas. O processo de desidrogenação do etanol na superfície m-ZrO_2(111) e no cluster Au_{13} ocorre por meio de duas etapas fundamentais: a clivagem inicial da ligação O–H no etanol, produzindo um intermediário CH_3CH_2O, seguido pela formação de H_2. A dissociação da ligação O–H ocorre por meio de interações com o oxigênio da rede na superfície do m-ZrO_2(111) ou com átomos de Au de baixa coordenação no cluster Au_{13}. Embora a modelagem microcinética revele constantes de taxa relativamente baixas para esse caminho, o composto Au_{13}/m-ZrO_2(111) introduz uma etapa adicional na qual um átomo de hidrogênio migra da superfície m-ZrO_2(111) para o cluster Au_{13}. Apesar dessa etapa adicional, nossa análise mostra que as energias de ativação para todos os três estados de transição são comparáveis, com o sistema Au_{13}/m-ZrO_2(111) demonstrando barreiras de energia mais baixas e constantes de taxa mais favoráveis para a desidrogenação do etanol. Essas descobertas destacam o potencial dos aglomerados de Au_{13} suportados em m-ZrO_2(111) para a produção eficiente e seletiva de CH_3CHO e H_2, oferecendo percepções importantes para o projeto de sistemas catalíticos avançados.

Abstract

UNRAVELING THE MECHANISM OF CH3CH2OH DEHYDROGENATION ON m-ZrO_2(111) SURFACE, Au_{13} CLUSTER, AND Au_{13} CLUSTER/m-ZrO_2(111) SURFACE: A DFT AND MICROKINETIC MODELING STUDY. In this study, we investigate the dehydrogenation of ethanol and the production of CH_3CHO and H_2 on the m-ZrO_2(111) surface, an Au_{13} cluster, and Au_{13}/m-ZrO_2(111) surface, using density functional theory simulations. Our primary objective is to elucidate the reaction mechanisms through thermodynamic and kinetic analysis of these catalytic processes, identifying the transition states. To further validate these findings, we employ a microkinetic model to calculate the rate constants, offering a detailed and comprehensive understanding of the reaction pathways involved. First-principles calculations were conducted using the Quantum ESPRESSO package, applying the BEEF-vdW functional for exchange and correlation interactions. The model systems were constructed in a two-dimensional supercell with periodic boundary conditions in the x and y directions, while a vacuum layer of 15 Å was introduced along the z direction to avoid interactions between periodic supercell slabs. The ethanol dehydrogenation process on both the m-ZrO_2(111) surface and the Au_{13} cluster proceeds via two fundamental steps: the initial cleavage of the O–H bond in ethanol, yielding a CH_3CH_2O intermediate, followed by the formation of H_2. The O–H bond dissociation occurs through interactions with lattice oxygen on the m-ZrO_2(111) surface or low-coordination Au atoms in the Au_{13} cluster. While microkinetic modeling reveals relatively low rate constants for this pathway, the Au_{13}/m-ZrO_2(111) composite introduces an additional step in which a hydrogen atom migrates from the m-ZrO_2(111) surface to the Au_{13} cluster. Despite this added step, our analysis shows that the activation energies for all three transition states are comparable, with the Au_{13}/m-ZrO_2(111) system demonstrating lower energy barriers and more favorable rate constants for ethanol dehydrogenation. These findings highlight the potential of Au_{13} clusters supported on m-ZrO_2(111) for efficient and selective production of CH_3CHO and H_2, offering key insights for the design of advanced catalytic systems.

Resumen

DESCUBRIENDO EL MECANISMO DE DESHIDROGENACIÓN DE CH_3CH_2OH EN LA SUPERFICIE m-ZrO_2(111), CLÚSTER DE Au_{13} Y SUPERFICIE DEL CLÚSTER Au_{13}/m-ZrO_2(111): UN ESTUDIO DE MODELADO DFT Y MICROQUINÉTICO. En este estudio, investigamos la deshidrogenación del etanol y la producción de CH_3CHO y H_2 en la superficie de m-ZrO_2(111), un cluster de Au_{13} y la superficie de Au_{13}/m-ZrO_2(111), utilizando simulaciones de teoría funcional de la densidad. Nuestro principal objetivo es dilucidar los mecanismos de reacción analizando la termodinámica y cinética de estos procesos catalíticos, identificando los estados de transición. Para dar mayor validez a estos resultados, empleamos un modelo microcinético para calcular las constantes de velocidad, ofreciendo una comprensión detallada y exhaustiva de las vías de reacción. Los cálculos de primeros principios se llevaron a cabo utilizando el paquete Quantum ESPRESSO, aplicando el funcional BEEF-vdW para las interacciones de intercambio y correlación. Los sistemas se construyeron en una supercelda bidimensional con condiciones de contorno periódicas en las direcciones x e y, mientras que se introdujo una capa de vacío de 15 Å a lo largo de la dirección z para evitar interacciones entre las placas periódicas de la supercelda. El proceso de deshidrogenación del etanol en la superficie m-ZrO_2(111) y en el cluster de Au_{13} tiene lugar a través de dos pasos fundamentales: la escisión inicial del enlace O–H en el etanol, produciendo un intermedio CH_3CH_2O, seguido de la formación de H_2. La disociación del enlace O–H se produce a través de interacciones con el oxígeno de la red en la superficie del m-ZrO_2(111) o con átomos de Au de baja coordinación en el clúster de Au_{13}. Aunque la modelización microcinética revela constantes de velocidad relativamente bajas para esta vía, el compuesto Au_{13}/m-ZrO_2(111) introduce un paso adicional en el que un átomo de hidrógeno migra desde la superficie de m-ZrO_2(111) hasta el clúster de Au_{13}. A pesar de esta complejidad adicional, nuestro análisis muestra que las energías de activación para los tres estados de transición son comparables, con el sistema Au_{13}/m-ZrO_2(111) demostrando barreras energéticas más bajas y constantes de velocidad más favorables para la deshidrogenación del etanol. Estos resultados ponen de manifiesto el potencial de los clústeres de Au_{13} soportados sobre m-ZrO_2(111) para la producción eficiente y selectiva de CH_3CHO y H_2, ofreciendo importantes perspectivas para el diseño de sistemas catalíticos avanzados.

Table of Contents

CHAPTER 1

1.1 – General Overview

The rapid growth of the global population, coupled with the escalating impacts of climate change, introduces substantial challenges for energy security and the future of the sustainability of our planet. Shifting toward fossil-free approaches for fuel and chemical production is crucial to lowering carbon dioxide emissions and securing the essential raw materials needed for manufacturing of several products. As projected by the International Renewable Energy Agency, bioenergy could supply between 7.5% and 37% of global energy production by 2050[1]. Alcohols serve as valuable feedstocks in yielding hydrogen and essential chemical building blocks such as aldehydes and ethers. Among alcohols, ethanol is widely available at competitive prices, with global production exceeding 120 million tons annually, and holds potential for cost-effective and environmentally friendly production via fermentation of syngas and other waste gases. Ethanol has emerged as a key chemical platform that is pivotal in sustainable energy and value-added chemical production. It can be upgraded into various intermediates such as ethylene, acetaldehyde, acetone, and hydrogen[2,3]. Acetaldehyde, a critical industrial product, is a precursor to numerous fine and bulk chemicals[4]. The conventional Wacker-Hoechst process currently produces acetaldehyde through the oxidation of ethylene in the presence of palladium and copper chloride[4]. However, developing alternative, ethanol-based pathways is essential for achieving more sustainable chemical production, though stable and robust catalysts for this application remain scarce[5].

Dehydrogenation reactions are fundamental for increasing the value of reactant molecules, producing essential dehydrogenated compounds, including hydrogen, a recognized green energy source. Alcohol dehydrogenation reactions can be categorized into two types: oxidative dehydrogenation, which uses oxygen to activate the alcohol and yields aldehydes and water, and non-oxidative dehydrogenation, where the alcohol acts as the sole reactant, producing aldehydes and hydrogen. Despite ethanol simple molecular structure, containing C−C, C−H, C−O, and O−H bonds, non-oxidative dehydrogenation is more challenging as it requires higher activation energy and selective cleavage of C−H and O−H bonds[6]. This process must minimize the formation of undesired by-products, such as CO, CH_4, H_2O, and coke, which can deactivate the catalytic active sites. A major challenge in ethanol dehydrogenation is catalyst deactivation, primarily caused by coking, which leads to the blockage of active sites[7]. Over the past decade, significant progress has been made in catalyst design, with innovative strategies aimed at overcoming this challenge. Recent studies on catalyst synthesis and characterization have shown the influence of preparation methods on catalyst structure and performance. Increasingly, research is focusing on how controlled synthesis techniques can regulate active sites, and the catalytic behavior in across reactions at different temperatures. Iwasa and Takezawa[8] investigated the influence of various supports, including SiO_2, ZrO_2, Al_2O_3, MgO, and ZnO, on the selectivity of Cu-based catalysts towards acetaldehyde or ethyl acetate. Their findings highlighted ZrO_2 as a particularly effective structural promoter, capable of preventing the sintering of Cu crystallites under reaction conditions. This property positions ZrO_2 as a promising alternative support material for enhancing catalyst stability and performance[9,10]. In addition, the activity of Cu/ZrO_2 catalysts has been found to strongly depend on the phase structure of ZrO_2. Specifically, Cu catalysts supported on monoclinic ZrO_2 (m-ZrO_2) have been reported[11] to exhibit higher activity in methanol synthesis compared to those supported on tetragonal ZrO_2 (t-ZrO_2), despite having the same Cu surface density. This difference has been attributed to the higher concentration of anionic defects present in m-ZrO_2 relative to t-ZrO_2[12]. Furthermore, the distinct spacing and symmetry of the Zr–O and –OH bonds in t-ZrO_2 and m-ZrO_2 are believed to play crucial roles in determining the dispersion of the active metal component and the overall catalytic behavior of the Cu/ZrO_2 system[12].

Zirconia is one of the most important metal oxides owing to its outstanding properties such as high dielectric constant, mechanical properties, high chemical and thermal stabilities, and wide band gaps. ZrO_2 exists in three distinct polymorphs, each stable within a specific temperature range. The monoclinic phase (m-ZrO_2) is predominant at temperatures below 1150 °C, the tetragonal phase (t-ZrO_2) is stable between 1150 and 2370 °C, and the cubic phase (c-ZrO_2) emerges at temperatures above 2370 °C[13]. Among these, m-ZrO_2 is the most thermodynamically stable phase, making it the preferred form for many catalytic applications due to its stability under various conditions. Known for its tunable acidic and basic surface sites, ZrO_2 facilitates the selective cleavage of C–H and O–H bonds in ethanol, promoting the production of acetaldehyde and hydrogen while minimizing undesired by-products such as CO, CH_4, and coke. Its excellent thermal stability makes it well-suited for high-temperature reactions, while its high oxygen storage capacity and mobility support oxidative processes, reducing catalyst deactivation. Furthermore, ZrO_2 exhibits strong metal-support interactions enhance the dispersion and stabilization of metal nanoparticles, preventing sintering and maintaining catalytic activity over time. These properties, combined with ZrO_2 low reactivity with hydrogen, make it an ideal choice for improving catalyst efficiency, and selectivity in ethanol dehydrogenation processes.

Noble metal nanoparticles are extensively studied in heterogeneous catalysis due to their high specific surface areas and abundant active centers[14–16]. The size of the nanoparticles is a crucial factor in determining catalyst performance. For many years, bulk gold was considered the most stable of all metals and regarded as an inert catalyst. However, gold nanoparticle (Au NPs) on the nanometer scale have proven surprisingly active and highly effective as green catalysts, making them a prominent research topic in heterogeneous catalysis[17,18]. Au clusters with diameters of 1 to 3 nm, consisting of specific numbers of metal atoms and ligands, have attracted significant attention for their unique physicochemical properties[19,20]. These properties are influenced by size effects, surface geometric effects (such as atom arrangement and low-coordinated atoms), and a high surface-to-volume ratio[21,22]. ZrO_2 is frequently employed as a support for gold-based catalysts, where gold is dispersed as clusters or nanoparticles, significantly enhancing catalytic performance. This system is utilized in key reactions such as the water–gas shift (WGS) reaction, methanol synthesis from CO_2 and H_2, CO oxidation, and the selective hydrogenation of 1,3-butadiene. ZrO_2 plays a crucial role in stabilizing gold species, thereby improving catalyst stability and activity across these diverse applications. Flytzani-Stephanopoulos *et al.*[23] investigated ethanol dehydrogenation over ZrO_2 and atomically dispersed gold supported on ZrO_2. Their study revealed that in temperature-programmed surface reactions (EtOH + H_2O-TPSR) on ZrO_2, shown that ethylene is the primary product, with the reaction initiating at approximately 300 °C and reaching complete ethanol conversion near 350°C. However, introducing 1 wt % of gold onto ZrO_2 lowered the ethanol conversion temperature to 200–250 °C, promoting the selective formation of acetaldehyde and hydrogen, while ethylene production only occurred at higher temperatures (400–450 °C). In a recent study, Bueno *et al.*[24] explored the effects of gold loading and pretreatment conditions on the catalytic activity of Au-supported m-ZrO_2 for ethanol dehydrogenation. They found that lower pretreatment temperatures resulted in smaller Au cluster sizes and the formation of low-coordinated Au sites. Catalysts pretreated at lower temperatures exhibited nearly double the reaction rate for acetaldehyde production compared to those treated at higher temperatures. These findings underscore the critical role of pretreatment conditions and gold dispersion in optimizing catalytic performance.

However, the catalytic conversion of ethanol entails a complex cascade of elementary reactions, and a comprehensive understanding of the underlying reaction mechanisms remains elusive.

1.2 – Publications

1.2.1 – Publication of the thesis

de Morais, L. H., López-Castillo, A., Andrés, Juan. Unraveling the mechanism of CH_3CH_2OH dehydrogenation on m-ZrO_2(111) surface, Au_{13} cluster, and Au_{13}/m-ZrO_2(111) surface: a DFT and microkinetic modeling study. *Applied Surface Science*, **680**, 161418, 2024.

1.2.2 – Other Publication

Osmari, T. A., Petrolini, D. D., López-Castillo, A., **de Morais, L. H.**, Zanchet, D., Sainna, M. A., Willock, D., Gallo, J. M. R., dos Santos, J. B. O, Bueno, J. M. C. Size-Dependent Effects of Cu Nanoparticles on Electronic Properties and Ethanol Dehydrogenation Catalysis Via Cu-O-Cu Species. *Materials Today Chemistry,* **41**, 4882301, 2024.

1.2 – Objectives

This thesis aims to develop a realistic model system based on the m-ZrO_2(111) surface, Au_{13} cluster, and Au_{13} cluster/m-ZrO_2(111) surface, investigate the reaction mechanisms involved in the ethanol dehydrogenation to formation of acetaldehyde and hydrogen, with particular attention to the performance of catalysts. Our primary aim is to elucidate the underlying reaction mechanisms facilitated by these catalysts. We employed density functional theory (DFT) to obtain thermodynamic and kinetic information regarding the reactions, including insights into transition states. A microkinetic model is also utilized to get the rate constants for these reactions. Regarding the interactions, we aim to elucidate the detailed pathways of the catalytic processes occurring on the m-ZrO_2(111) surface, Au_{13} cluster, and Au_{13} cluster/m-ZrO_2(111) surface, thereby enhancing our understanding of their catalytic behavior.

CHAPTER 2

2.1 – Theoretical Background

This chapter will cover the theories behind the work done in this project: Density functional theory, adsorption energy, Bader analysis, and nudged elastic band calculations.

2.2 - Density Functional Theory

The primary goal of first-principles methodologies is to resolve the electronic structure of atoms and molecules in a chemical system by solving the many-body Schrödinger equation. To make this computationally feasible, approximations like the Born-Oppenheimer approximation[25] are employed, where the motion of electrons and nuclei is decoupled. This approximation is justified by the significant mass disparity between electrons and nuclei, where even the lightest nucleus is orders of magnitude heavier than an electron, allowing the assumption that nuclear motion remains stationary relative to the rapid motion of electrons.

The Schrödinger equation is given by:

$$\hat{H}\psi = E\psi \qquad (2.1)$$

Where ψ is the wave function of the system, H denotes the Hamiltonian operator, E correspond to the energy of the system. The Hamiltonian is:

$$\hat{H} = \hat{T}_e + \hat{V}_{ne} + \hat{V}_{ee}. \tag{2.2}$$

The kinetic energy, $\hat{T}_e$ of the N electrons in the system is represented by:

$$\hat{T}_e = -\frac{1}{2}\sum_{i=1}^{N} \nabla_i^2. \tag{2.3}$$

The operator ∇_i^2 is the Laplacian, which acts on the coordinates of the electrons, is defined as:

$$\nabla_i^2 = \frac{\partial^2}{\partial x_i^2} + \frac{\partial^2}{\partial y_i^2} + \frac{\partial^2}{\partial z_i^2} \ . \tag{2.4}$$

The potential energy of nucleus-electron, $\hat{V}ne$, is given by:

$$\hat{V}_{ne} = -\sum_{\alpha=1}^{M} \sum_{i=1}^{N} \frac{1}{4\pi\varepsilon_0} \frac{Z_\alpha e^2}{|\vec{R}_\alpha - \vec{r}_i|} \ . \tag{2.5}$$

In this expression, R_α and r_i represent the nuclear positions and electronic positions, respectively.

And the potential energy of electron-electron, $\hat{V}ee$, is given by:

$$\hat{V}_{ee} = \sum_{i=1}^{N} \sum_{j>i}^{N} \frac{1}{4\pi\varepsilon_0} \frac{e^2}{|\vec{r}_i - \vec{r}_j|} \ . \qquad (2.6)$$

2.2.1 – The Hohenberg-Kohn Theorems

The Hohenberg-Kohn theorems, published in 1964 by Pierre Hohenberg and Walter Kohn[26], are the basis of the DFT. In the first theorem, established that the ground state density of a many-electron system is uniquely determined, except for an additive constant, from the external potential.

The second theorem establishes that the energy of the ground state corresponds to the minimum of the energy functional, $E_0[\rho_0(r)]$, obtained from the exact density of the ground state, $\rho_0(r)$. Any different density will lead to an energy greater than the energy of the ground state, $E[\rho'(r)] > E_0[\rho_0(r)]$. This theorem enables the application of the variational principle to determine the ground-state density by identifying the density configuration that minimizes the system energy, finding the ground-state density.

2.2.2 – The Kohn-Sham Equations

Kohn and Sham 1965 reformulated the problem of calculating the total electronic energy by introducing a concept that greatly simplified the many-body problems. They proposed that, instead of solving the complex many-body Schrödinger equation, the system could be described exactly by a set of non-interacting electrons moving in an effective potential. This approach allows the total energy of the system to be computed as the sum of the kinetic energy of these non-interacting electrons, the classical electrostatic energy, and an additional exchange-correlation energy term. Applying the variational principle that the density minimizes the total energy functional, we may vary the non-interacting system until the functional is minimized and arrive at the charge density and energy of the real interacting electron system. This variation gives rise to a set of Euler–Lagrange equations that govern the single-particle orbitals and energies of the non-interacting system.

$$\left[-\frac{\hbar}{2m}\nabla^2 + V_{eff}(r)\right]\varphi_i(r) = \varepsilon_i\varphi_i(r) \, , \qquad (2.7)$$

with:

$$\rho(r) = \sum_i^{occc} |\varphi_i(r)|^2 \, . \qquad (2.8)$$

The effective potential, V_{eff} is defined as:

$$V_{eff}(r) = V_H(r) + V_{XC}(r) + V_{ext}(r) \; . \qquad (2.9)$$

The Hartree potential is defined as:

$$V_H(r) = \int \frac{\rho(r\prime)}{|r-r'|} dr' \; . \qquad (2.10)$$

and V_{XC}:

$$V_{XC}(r) = \frac{\delta E_{XC}}{\delta \rho(r)} \ . \qquad (2.11)$$

In which, if E_{xc} were known, a self-consistent solution to the Kohn– Sham equations would give the exact electron density and ground-state energy of the interacting system as a function of the atomic coordinates and hence also a host of other properties that are related to the ground state. Since E_{xc} is unknown, approximations must be made:

$$E_{XC} = \int \rho(r)\varepsilon_{XC}(r)\, dr. \qquad (2.12)$$

Where $\varepsilon_{XC}(r)$; a local exchange-correlation energy density, is assumed to be a function of the local density $\rho(r)$ in the local density functional approximation (LDA) or a function of $\rho(r)$and $\nabla\rho(r)$in the generalized gradient approximation (GGA)[27].

2.2.3 - **Bayesian Error Estimate Functional with van der Waals dispersions**

The Bayesian Error Estimate Functional (BEEF-vdW), developed by Wellendorff *et al.*[28] presents a fitted GGA functional, containing a portion of the non-local vdW-DF2 kernel, in which form and parameters are primarily determined through theoretical considerations. The correlation term is expanded more simply, with only a single parameter, as a combination of LDA correlation E_c^{LDA} and PBE correlation E_c^{PBE}.

The E_c^{LDA} parametrized by Perdew and Zunger is written as:

$$E_c^{LDA} = \begin{cases} -\frac{0.1423}{1+1.9529\sqrt{\frac{r_s}{a_0}}+0.334\frac{r_s}{a_0}};\ r_s \geq 1 \\ -0.048 + 0.0311 ln\frac{r_s}{a_0} - 0.0116\frac{r_s}{a_0} + 0.002 r_s ln\frac{r_s}{a_0};\ r_s < 1 \end{cases}$$

(2.10)

Where the r_s represents the Wigner-Seitz radius and a_0 Bohr radius:

$$r_s = \left[\left(\frac{4\pi}{3}\rho\right)\right]^{-\frac{1}{3}} , \qquad (2.11)$$

$$a_0 = \epsilon_0 \frac{h^2}{\pi m e^2} . \qquad (2.12)$$

The parameter ρ can be interpreted as the mean electronic density within the outer region of the Wigner-Seitz cell. In the Bohr radius, ϵ_0 is the vacuum permittivity constant and h is Planck's constant; m and e are, respectively, the mass and charge of the electron.

And the E_c^{PBE} is written as:

$$E_c^{PBE} = \int d^3 r n\left[\epsilon_c^{uni}(r_s) + H(r_s, t)\right] . \qquad (2.13)$$

Whereby $\epsilon_c^{uni}(r_s)$ is the correlation energy per particle at uniform electron gas, H is the contribution of the correlation gradient, and t is a dimensionless gradient of the density.

The representation of the exchange energy in BEEF-vdW is written as follows:

$$E_x[\rho] = \sum_m a_m B_m(t(s)) . \qquad (2.14)$$

the term $B_m$denotes the Legendre polynomial of order m, and t(s) is a modification of the reduced density gradient, in which is given by:

$$t(s) = \frac{2s^2}{4+s^2} - 1, t \in [-1,1] \ . \tag{2.15}$$

Where the value of 4 was chosen for simplicity, while still matching the PBE form. Using the definition of the exchange functional in the generalized gradient approximation (GGA), the expanded exchange energy can be expressed as follows:

$$E_x^{GGA}[n, \nabla n] = \sum_m a_m \int \epsilon_x^{LDA} B_m\big(t(s)\big)\, n(r) dr \tag{2.16}$$

and the correlation energy

$$E_c[n, \nabla n] = \alpha_c E_c^{LDA} + (1 - \alpha_c) E_c^{PBE} + E_c^{nl} \tag{2.17}$$

with E_c^{nl}being the non-local vdW-DF2 correlation energy. By combining the exchange and correlation contributions, the BEEF-vdW functional is represented as follows:

$$E_{xc} = \sum_{m=0} a_m \int \epsilon_x^{LDA} B_m\big(t(s)\big)\, n(r) dr + \alpha_c E_c^{LDA} + (1 - \alpha_c) E_c^{PBE} + E_c^{nl} \tag{2.18}$$

2.3 – Periodic Systems

Analogous to the crystal lattice, one can construct a single cell of the reciprocal lattice, typically defined as a Wigner-Seitz cell centered on a chosen origin point within the reciprocal lattice. A reciprocal lattice corresponding to a crystal lattice is defined by a set of vectors G_m that satisfy the relation:

$$R_n . G_m = 2\pi \times \text{Z} \qquad (2.19)$$

where Z represents an integer number, for all translation vectors of the crystal lattice, denoted as R_n, the set of vectors G_m represents the translation vectors of the reciprocal lattice, defining the points within this lattice. This unit cell retains all the symmetry properties inherent to the reciprocal lattice and is referred to as the first Brillouin zone. According to Bloch's theorem, the electronic description of a system can be effectively reduced to the wave vectors located within the first Brillouin zone. This is because the plane waves characterized by the k vectors of the reciprocal lattice exhibit the same periodicity as the lattice itself.

Recognizing that atoms are arranged in a periodic pattern within solids, any quantity of interest that depends on r is also periodic. Consequently, the potential acting on the electrons can be considered periodic and invariant under translation by a real lattice vector R.

$$U(R) = U(r + R) \qquad (2.20)$$

Where R is the real lattice vector defined by $R = n_1a_1 + n_2a_2 + n_3a_3$, in which n_i = integer number, and a_i = unit cell vectors. Similarly, the electron density in a periodic solid is periodic, as it also depends on the position r.

$$\rho(r) = \rho(r + R) \qquad (2.21)$$

Bloch mapped out the planewaves onto the structurally repeating pattern of a solid and made the wave functions quasi-periodic with the introduction of a cell periodic, $u_k(r)$:

$$\Psi_k(r) = u_k(r).e^{(ik.r)} \quad (2.22)$$

where $u_k(r)$ is a periodic function. Knowing that any periodic function in a finite real space can be expanded as a Fourier series using plane waves based on the reciprocal lattice vector G, we can apply this to $u_k(r)$ in three dimensions. This results in the following expansion:

$$u_k(r) = \sum_G C_k(G)e^{(iG.r)} \quad (2.23)$$

where $C_k(G)$ is the Fourier expansion coefficients of the wave functions that replace the real-space values of wave functions. The phase factor, $e^{(iG.r)}$, associated with each G represents a plane wave traveling in space, oriented perpendicular to the vector G. Utilizing the equation 2.23 in 2.22, the wave function can be written as:

$$\begin{aligned} \Psi_k(r) &= u_k(r).e^{(ik.r)} \\ &= \sum_G C_k(G)e^{(iG.r)}e^{(ik.r)} \quad (2.24) \\ &= \sum_G C_k(G)e^{[i(k+G).r]} \end{aligned}$$

Replacing the equation 2.24 in the equation 2.7 and multiply both sides by $e^{(-ik.r)}$ we obtain:

$$-\frac{1}{2}\nabla^2 e^{-ik.r}\left[e^{ik.r}u_{ik}(r)\right] + V_s(r)u_{ik}(r) = \varepsilon_{ik}u_{ik}(r) \quad (2.25)$$

Which leads to:

$$\left[-\frac{1}{2}(\nabla + ik)^2 + V(r)\right] u_{ik}(r) = \varepsilon_{ik} u_{ik}(r) \qquad (2.26)$$

In this formulation of the Kohn–Sham equations, the complex $e^{(ik.r)}$ has been eliminated, leaving the function to be determined as solely the periodic part u_{ik} of the Kohn–Sham state. This outcome can be expressed that the periodic component of the Kohn–Sham wavefunction is an eigenstate of a modified Hamiltonian, $\hat{H}_{KS}$:

$$\hat{H}_{KS} u_{ik} = \varepsilon_{ik} u_{ik} \ , \quad \hat{H}_{KS} = -\frac{1}{2}(\nabla + ik)^2 + V_s \qquad (2.27)$$

2.4 – Projector Augmented Wave Method

The Projector Augmented Wave (PAW) method was developed to effectively describe the rapid oscillations of plane wave functions near the nucleus, allowing for a clear separation between the valence regions and the regions adjacent to the core. This method divides the regions into two distinct areas: the core, where the electronic structure is treated with high precision using pseudopotentials to represent the nuclei and valence electrons; and an augmented region, where augmented plane wave functions are employed to represent the innermost electrons. Following the addition of these two components, the overlapping part Ψ_{net} is removed, resulting in the final wave function Ψ_{PAW}, which closely approximates the all-electron wave function.

$$\Psi_{PAW} = \Psi_{valence} + \Psi_{core} - \Psi_{net} \ . \qquad (2.28)$$

Thus, the PAW method yields results that are as accurate as those obtained from the all-electron full-potential approach, while requiring significantly less computational effort.

2.5 – Adsorption Energy

The adsorption energy (E_{ads}) is determined by the total energy difference between the combined system of the catalyst surface and the adsorbed molecule ($E_{slab+molecule}$) and the individual energies of the isolated catalyst surface (E_{slab}) and the free molecule ($E_{molecule}$), according to the following equation:

$$E_{ads} = E_{slab+molecule} - E_{slab} - E_{molecule} \; . \qquad (2.29)$$

For adsorption to occur spontaneously, the adsorption energy must be negative, indicating stabilization of the system. The surface with the adsorbed molecule, the isolated surface, and the free molecule must be simulated using consistent convergence and accuracy criteria for valid comparison.

2.6 – Bader Analysis

The chemical properties of atoms and molecules are fundamentally influenced by their electric charges. Richard Bader, developed an intuitive way of dividing molecules into atoms called the Quantum Theory of Atoms in Molecules (QTAIM). This analysis uses what are called zero flux surfaces to divide atoms, as presented in equation 2.19:

$$\nabla\rho(r).\hat{n}(r) = 0 \; . \qquad (2.30)$$

where $\hat{n}(r)$ is the unit vector normal to the surface $S(\Omega,\mathbf{r})$ at point $\boldsymbol{r}$. The spatial domain is systematically partitioned into distinct regions, known as Bader regions, delineated by surfaces that traverse the minima in the charge density. Each Bader region is typically associated with a single atom, allowing for a clear charge assignment. By integrating the charge density within each defined region, it is possible to calculate the total charge contained in that section, thereby determining the effective charge on the corresponding atom.

2.7 – Nudged Elastic Band

Several methods have been developed to identify transition states on potential energy surfaces (PES), primarily aimed at locating first-order saddle points within the harmonic transition state theory framework. Among the most widely used techniques are the Drag method and the nudged elastic band (NEB) method, which facilitate determining reaction pathways by optimizing configurations along the transition state. Other methods include the dimer method and the freezing string method, each offering unique advantages for exploring the energy landscape and enhancing the accuracy of transition state characterization. These approaches elucidate reaction mechanisms and activation barriers, providing insights critical for understanding the chemical kinetics and dynamics of the reaction.

The NEB method, mainly its variant known as the climbing-image NEB (CI-NEB), has emerged as a standard approach for locating transition states on PES. This method involves the relaxation of a series of images along a presumed reaction path to effectively identify the first-order saddle point.

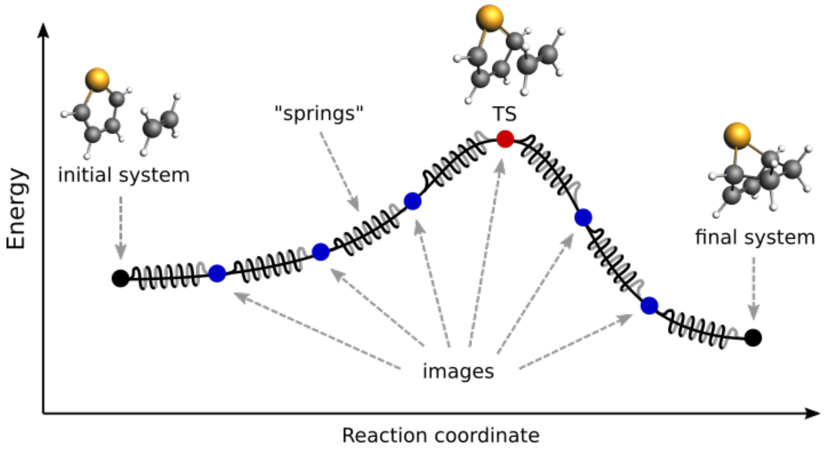

Figure 1. Representation of a reaction path with CI-NEB. Adapted from Amsterdam Modeling Suite[29].

CHAPTER 3

UNRAVELING THE MECHANISM OF CH_3CH_2OH DEHYDROGENATION ON m-ZrO_2(111) SURFACE, Au_{13} CLUSTER, AND Au_{13} CLUSTER/m-ZrO_2(111) SURFACE: A DFT AND MICROKINETIC MODELING STUDY (APPLIED SURFACE SCIENCE – IMPACT FACTOR 6.3)

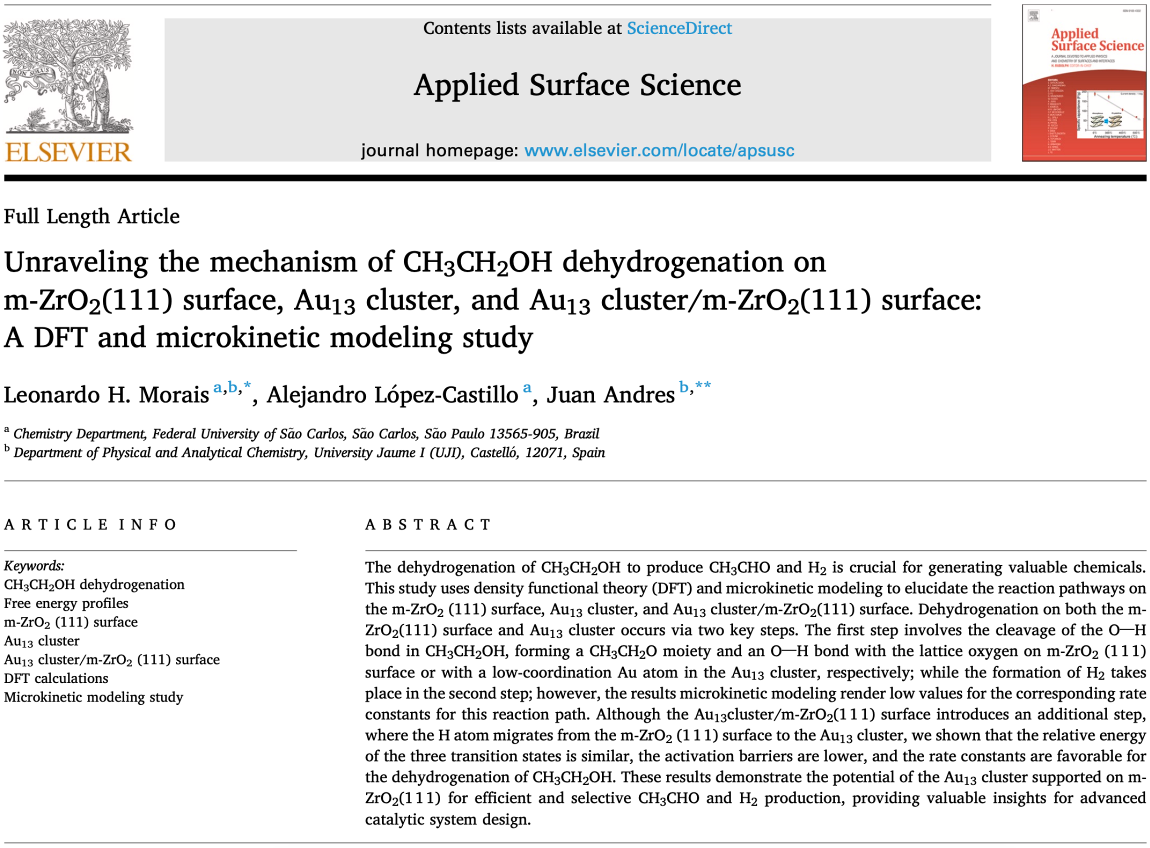

Contents lists available at ScienceDirect
Applied Surface Science
journal homepage: www.elsevier.com/locate/apsusc

Full Length Article

Unraveling the mechanism of CH_3CH_2OH dehydrogenation on m-ZrO_2(111) surface, Au_{13} cluster, and Au_{13} cluster/m-ZrO_2(111) surface: A DFT and microkinetic modeling study

Leonardo H. Morais [a,b,*], Alejandro López-Castillo [a], Juan Andres [b,**]

[a] *Chemistry Department, Federal University of São Carlos, São Carlos, São Paulo 13565-905, Brazil*
[b] *Department of Physical and Analytical Chemistry, University Jaume I (UJI), Castelló, 12071, Spain*

ARTICLE INFO

Keywords:
CH_3CH_2OH dehydrogenation
Free energy profiles
m-ZrO_2 (111) surface
Au_{13} cluster
Au_{13} cluster/m-ZrO_2 (111) surface
DFT calculations
Microkinetic modeling study

ABSTRACT

The dehydrogenation of CH_3CH_2OH to produce CH_3CHO and H_2 is crucial for generating valuable chemicals. This study uses density functional theory (DFT) and microkinetic modeling to elucidate the reaction pathways on the m-ZrO_2 (111) surface, Au_{13} cluster, and Au_{13} cluster/m-ZrO_2(111) surface. Dehydrogenation on both the m-ZrO_2(111) surface and Au_{13} cluster occurs via two key steps. The first step involves the cleavage of the O—H bond in CH_3CH_2OH, forming a CH_3CH_2O moiety and an O—H bond with the lattice oxygen on m-ZrO_2 (1 1 1) surface or with a low-coordination Au atom in the Au_{13} cluster, respectively; while the formation of H_2 takes place in the second step; however, the results microkinetic modeling render low values for the corresponding rate constants for this reaction path. Although the Au_{13}cluster/m-ZrO_2(1 1 1) surface introduces an additional step, where the H atom migrates from the m-ZrO_2 (1 1 1) surface to the Au_{13} cluster, we shown that the relative energy of the three transition states is similar, the activation barriers are lower, and the rate constants are favorable for the dehydrogenation of CH_3CH_2OH. These results demonstrate the potential of the Au_{13} cluster supported on m-ZrO_2(1 1 1) for efficient and selective CH_3CHO and H_2 production, providing valuable insights for advanced catalytic system design.

3.1 - Introduction

Ethanol (CH_3CH_2OH) dehydrogenation to yield acetaldehyde (CH_3CHO) and hydrogen (H_2) has received significant attention as a promising, highly efficient production process of value-added chemicals under mild conditions and in a sustainable manner[30–32]. CH_3CHO is mainly produced using the Hoesch-Wacker process from ethylene oxidation, derived from the steam-cracking of fossil fuels. The CH_3CHO market was worth US$1.26 billion in 2016[33], and it is expected to grow to 1.6 million tons by 2024[34] and an estimated US$2.1 billion by 2027[35]. It is widely employed in sectors such as food, plastics, the manufacturing of acetic acid, paint binders in alkyd paints, and as a component or in the production of materials in several areas, such as the civil, pharmaceutical, and cosmetics industries[36,37]. Furthermore, it is crucial in converting CH_3CH_2OH to CH_2CHCH_3[38], $C_4H_{10}O$ [39], C_4H_6 [40], C_4H_8[41], and aromatics[42]. The non-oxidative dehydrogenation of CH_3CH_2OH produces H_2, making it more profitable for large-scale CH_3CHO production[43].

The direct dehydrogenation of CH_3CH_2OH still faces many technological and economic challenges[44,45]. Zirconia, ZrO_2, has been extensively investigated among oxide support catalysts due to its properties such as thermal stability, chemical stability, and high specific area[46]. Uphade *et al.*[47] studied the influence of metal oxide support on the catalytic activity and selectivity in the oxidation of benzyl alcohol to benzaldehyde. They reported that Au/ZrO_2 has higher activity, suggesting an excellent catalyst for converting alcohol to aldehyde. Flytzani-Stephanopoulos *et al.* [23] investigated the catalytic activity and selectivity using temperature-programmed surface reactions. They showed that the principal product of CH_3CH_2OH conversion on the ZrO_2 surface is ethylene, and adding Au on the ZrO_2 surface modifies surface acidity, increasing selectivity to produce CH_3CHO. Although unsupported Au is unreactive[48], when covered with atomic oxygen, Au became catalytic active[49,50], albeit less active than supported Au catalysts[51]. The rational design of metal oxide-supported Au catalysts has already been shown to be active and selective for CH_3CH_2OH dehydrogenation and efficient generation of the desired products[52–55]. It is known that the reaction pathways on the catalyst surfaces depend on the metals and supports used [23,56–58]. Solymosi *et al.*[58] and Dalai *et al.*[59] studied the decomposition and reforming of

CH_3CH_2OH on supported Au catalysts, with particular emphasis on the effects of the supports. These authors reported that Au/ZrO_2 exhibits the highest hydrogen production in the temperature range between 210 and 300°C, which is related to the highest Au^0/Au^+ ratio and low surface acidity. On the other hand, Bueno *et al.*[24] observed that pretreatment in different temperatures could influence the density and reactivity, and monoclinic m-ZrO_2 did not exhibit CH_3CH_2OH conversion into CH_3CHO under reaction conditions, while Au supported on m-ZrO_2 was revealed to be a suitable catalyst for CH_3CH_2OH conversion and exhibits higher activity when prepared at lower temperatures, 200°C. In theoretical approaches, it is well-established that clusters with specific numbers of atoms, known as geometric "magic numbers," are more stable and abundant in typical cluster experiments. These magic numbers correspond to highly symmetric structures that confer enhanced stability and reactivity to the clusters[60]. In the case of Au, the ubiquitous icosahedral Au_{13} are widely studied due to their broad range of low-coordinated sites[61] and the flexibility of the cluster[62]. This flexibility can significantly affect the interactions at the cluster level, influencing both reactivity and stability, which are key factors in catalytic performance[63,64].

Understanding the nature of intermediates/transition structures active species in reactions is a major challenge in chemical reactivity. The investigation of chemical reactions using density functional theory (DFT) calculations is the commonly used procedure among the available computational methods due to its optimal compromise between accuracy and computational cost, allowing mechanistic insights at the atomic level, which are often inaccessible or masked to experiments. Therefore, gaining atomic-scale insights into the underlying molecular mechanism holds significant guidance for designing highly active catalytic sites and, furthermore, improving the catalytic performance. Herein, we present a systematic study of the CH_3CH_2OH dehydrogenation to yield CH_3CHO and H_2 on three models: monoclinic m-ZrO_2(111) surface, Au_{13} cluster, and Au_{13} cluster supported on monoclinic m-ZrO_2(111) surface, Au_{13} cluster/m-

ZrO_2(111) surface. The free energy profiles have been calculated, and the corresponding transition state (TS) and intermediate (I) have been characterized. The structure of reactive sites and the electron charge transfer processes are analyzed to disclose the reaction pathways associated with the chemical rearrangements. We focus primarily on answering two central questions: (i) How do the O-H bond breaking process of hydroxyl moiety of CH_3CH_2OH and H-H bond formation process occur along the reaction pathways? (ii) How are the free energy barriers along the reaction progress to render CH_3CHO and H_2? To the best of our knowledge, this is the first DFT study on the complete dehydrogenation of CH_3CH_2OH over these systems. The obtained results will contribute to interpreting the experimental results and provide the overall pathways and energetics of this chemical rearrangement. We expect not only to offer a more reasonable explanation for previous studies but also to provide guidance, which is essential for further improving the activity and selectivity of Au/ZrO_2 catalysts.

3.2 – Computational Methods and Model Systems

The DFT calculations were carried out using Quantum Espresso package[65] by using the projector-augmented wave (PAW) method[66]. BEEF-vdW[67] in the generalized gradient approximation (GGA) scheme exchange–correlation functional was selected with a kinetic energy cutoff of 30 Ry and a threshold for self-consistency of 10^{-5} eV.

The initial data for the bulk cell was obtained from the materials project for m-ZrO_2 (mp-2858). The lattice parameters obtained ($a = 5.18$, $b = 5.26$, and $c = 5.36$; $\beta = 99.49$) agree with experimental and theoretical data [68–71]. All Zr atoms are seven-fold coordinated, and two nonequivalent oxygen sites are threefold and fourfold coordinated. We cut the optimized bulk along the [111] direction to build our surface model with a perpendicular 15 Å vacuum in the z-axis direction. The proposed model was built with a 2x2 supercell that added equivalent atoms in symmetric positions along the x and y axes. Brillouin zone integration was performed using the Monkhorst– Pack method[72] with 2 × 2 × 1 k-points. The Au_{13} cluster was centered at 20 × 20 × 20 Å supercell with Γ point. The Au_{13} cluster/m-$ZrO_2(111)$ surface was built from the optimized previous monoclinic m-$ZrO_2(111)$ surface and Au_{13} cluster.

Transition states (TS) were characterized using the climbing image nudged elastic band (CI-NEB) method [73], with force convergence criteria of 0.5×10^{-1} eV/Å, and self-consistency of 10^{-5} eV. Eight intermediate images were used in these calculations, initially generated by the image-dependent pair potential method.[74] We find a single imaginary frequency for all transition states in the reaction, thus identifying the geometry as a first-order saddle point on the potential energy surface.

The relative Gibbs free energy values (G) reported in this work were evaluated by the expression:

$$G = E_{DFT} + ZPE + \int_0^T C_p \, dT - T\Delta S \,. \quad (1)$$

The values of zero-point energy (ZPE), entropy (ΔS), and heat capacity (C_P) were derived from the normal vibrational modes of the surface or adsorbed systems or gas-phase molecules considering the temperature of 473.15 K and pressure of 101.3 kPa when not explicitly indicated. Thus, the energy values obtained by DFT calculations at 0 K with the electronic smearing extrapolated to zero (E_{DFT}) were corrected[75].

As presented by Bendavid and Carter[75], at absolute zero and zero pressure, the internal energy and the enthalpy are equal. To account for enthalpy corrections at nonzero temperatures, the heat capacity must be integrated at constant pressure from absolute zero to the temperature of interest, so that the enthalpy is defined as:

$$H = E + ZPE + \int_0^T C_p(T')dT' \qquad (2)$$

And, the Gibbs free energy can be calculated by subtracting the contribution from entropy:

$$G = H - TS \qquad (3)$$

The Gibbs free energy of activation was estimated as $\Delta G_a = G_{TS} - G_{IS}$, in which G_{TS} is the free energy of the transition state, and G_{IS} is the free energy of the initial state. The reaction free energy was estimated as $\Delta G_r = G_{FS} - G_{IS}$, in which G_{FS} is the free energy of the final state.

The forward and backward rate constants of reactions were obtained by applying Eyring equation[76]. As shown in the following equation:

$$k = \frac{k_b T}{h}\frac{Q'}{Q}e^{-\frac{E_a}{k_b T}} \qquad (4)$$

Where h, T, Q', Q, and K_b represent the Planck constant, the temperature, the partition function of TS, the partition function of IS, and the Boltzmann constant, respectively. We evaluated the rate constants alongside activation energies to determine the most suitable catalyst for each reaction step. This analysis allows us to identify the catalysts with optimal performance based on their balance of low activation energy and high rate constants. These factors are crucial for guiding the selection of effective catalysts in the reaction mechanism.

We performed a Bader charge analysis[77] to obtain the electronic charge variation on the interacting systems during the reaction.

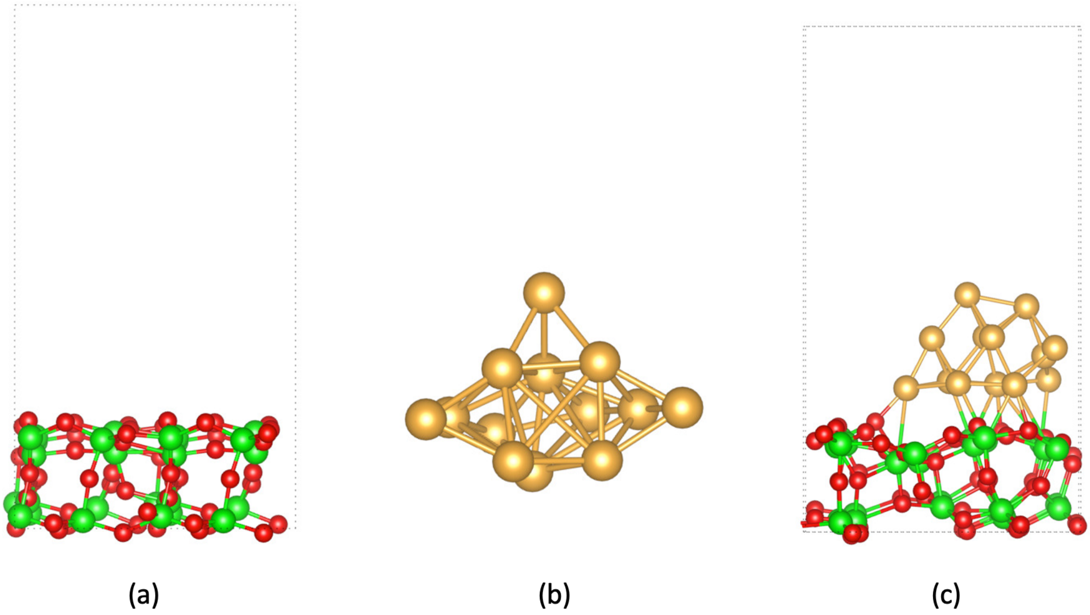

Figure 2. A schematic representation of the model systems. a) m-ZrO_2(111) surface (**I**), b) Au_{13} cluster (**II**), and c) Au_{13} cluster/m-ZrO_2(111) surface (**III**).

The m-ZrO_2(111) surface (**I**) present values of Zr-O bond lengths in the range from 2.10 to 2.35 Å, while Zr-O distance between Zr atom and O atom located in the adjacent layer decreases to 1.97 Å.

It is well known that Au clusters with size less than 2nm supported on oxide material showed efficiency in the evolution of the catalytic activities on Au catalysts[78,79]. Based on this fact, we have selected the Au_{13} cluster (**II**), which presents a close size. The average Au-Au bond length is 2.81 Å, in agreement with the literature[80].

To develop a realistic model of the Au_{13} cluster/m-ZrO_2(111) surface, we explored different interaction modes between both systems and selected the most stable configuration (see Fig. S1). In the Au_{13} cluster/m-ZrO_2(111) surface (**III**) model, the Au_{13} cluster interacts with Zr and O atoms of the m-ZrO_2(111) surface, and the range distances for the Au–Zr bond and Au–O bond are 3.08-3.49 Å and 2.24-2.37 Å, respectively. These values are consistent with the work of Puigdollers and Pacchioni[81], who studied reactions on the Au_{10}/ZrO_2(111) surface with Au–Zr and Au–O bond distances from 3.12 to 3.79 Å, and 2.11 to 2.16 Å, respectively. The average Au-Au bond length on the cluster supported decreased to 2.80 Å. The Zr-O bond length close to the cluster increases the range from 2.16 to 2.37 Å. Besides that, a charge transfer of 0.24 e was observed from the Au_{13} cluster to the m-ZrO_2(111) surface, where e is the charge of an electron.

3.3 – Results and Discussions

The calculated free energy profiles and the structures of the corresponding transition states and intermediates for the m-ZrO_2(111) surface, the Au_{13} cluster, and the Au_{13} cluster/m-ZrO_2(111) surface are depicted in Figures 2 and 3, Figures 4 and 5, and Figures 6 and 7, respectively. The reaction free energy (ΔG_r), activation free energy (ΔG_a) for each transition state, and the rate constants of the reactions are detailed in Tables 1, 2, and 3, respectively.

3.3.1 - CH_3CH_2OH Dehydrogenation Over m-ZrO_2(111) Surface

Adsorption of CH_3CH_2OH on the m-ZrO_2(111) surface occurs at the top of the Zr atom. The Zr–$O_{Ethanol}$ bond length at the initial adsorption intermediate (I_1-**I**) is 2.48 Å, with a reaction free energy (ΔG_r) of -0.99 eV. These values align closely with those reported by Chen *et al.* for CH_3CH_2OH dehydrogenation on the

ZrO_2(111) surface[82]. The charge transfer from CH_3CH_2OH to m-ZrO_2(111) is 0.02 e, indicating a weak interaction.

The adsorbed CH_3CH_2OH dissociates via the first transition state (TS_1-I), which involves the cleavage of the O-H bond of the hydroxyl group of CH_3CH_2OH, assisted by lattice oxygen, to form an O-H bond. This step shows a decrease of Zr–$O_{Ethanol}$ and αC-O bond lengths of 0.290 and 0.029 Å, respectively. A mild barrier height of 0.36 eV was observed, and the thermodynamics of the reaction favors the process, as indicated by the exothermic free energy of ΔG_r=0.21 eV. This was further confirmed by the rate constant of the reaction, where the forward reaction is three orders of magnitude higher than the backward reaction. In the second step, the breaking of the αC–H bond of CH_3CH_2O moiety and the formation of the H-H bond occurs via the transition state, TS_2-**I.** During this stage, the CH_3CH_2O moiety rotates to facilitate the interaction of H from the αC–H to the H bonded on the O from the ZrO_2(111) surface. With this, a decrease in Zr-O bond length was observed by 0.464 Å, while an increase of αC-O bond length by 0.170 Å can be sensed. The corresponding energy barrier ΔG_a is 1.79 eV, with an endothermic free energy of ΔG_r=0.40 eV. Despite the high energy barrier, the microkinetic rate constant indicates that the backward reaction is ten orders of magnitude higher than the forward reaction, confirming the unfavorable nature of the reaction. Su *et al.* [82] observed the cleavage of the αC-H bond is the limiting step in monoclinic ZrO_2 with a barrier energy of 1.79 eV. In contrast, Yu *et al.*[83], by using DFT calculations, observed that on a tetragonal ZrO_2(101) surface, the formation of H_2 required ΔG_a=2.08 eV and the reaction energy ΔG_r=1.68 eV.

In the intermediate I_3-**I**, the generation of H_2 and the adsorption of CH_3CHO on the m-ZrO_2(111) surface can be sensed. The αC-O bond length is reduced to 1.242 Å, and the Zr-O bond length decreases by 0.293 Å, exhibiting similar bond lengths and adsorption energy to those observed in intermediate I_1-**I**. Finally, the desorption energy of CH_3CHO on the m-ZrO_2(111) surface was determined to be 0.75 eV.

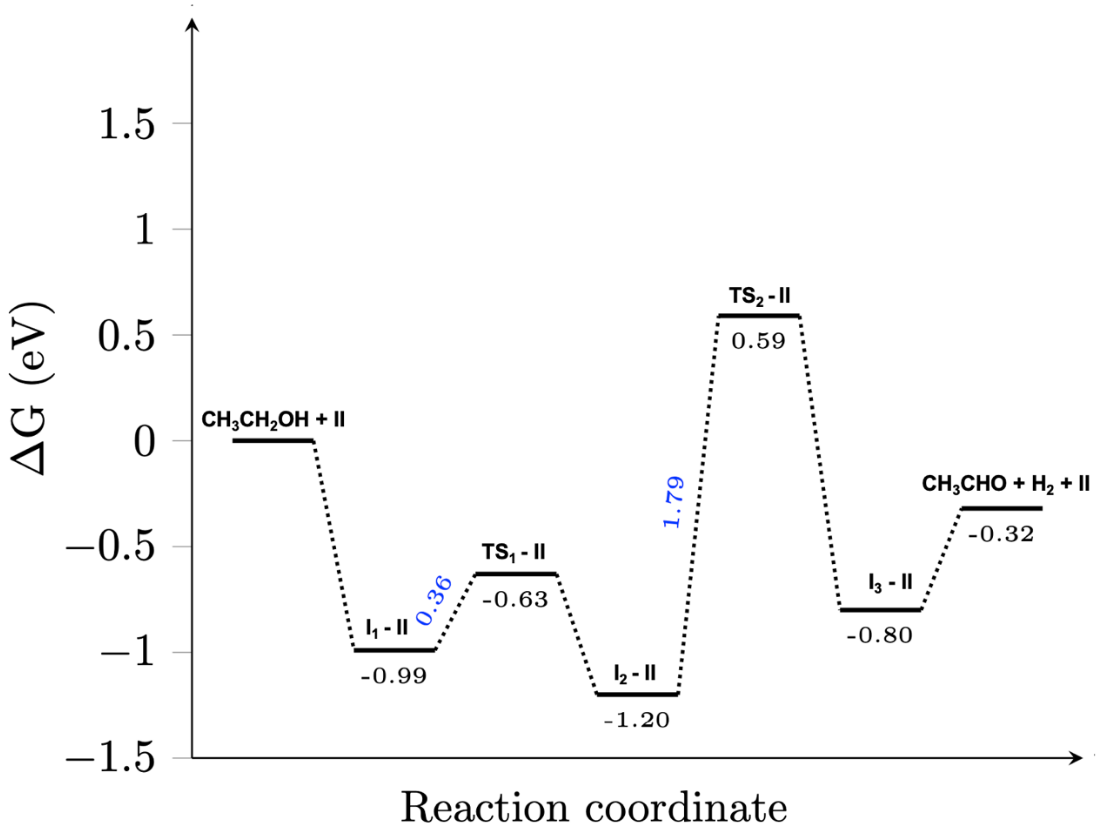

Figure 3. The calculated free energy profile of CH_3CH_2OH dehydrogenation on the m-ZrO_2(111) surface.

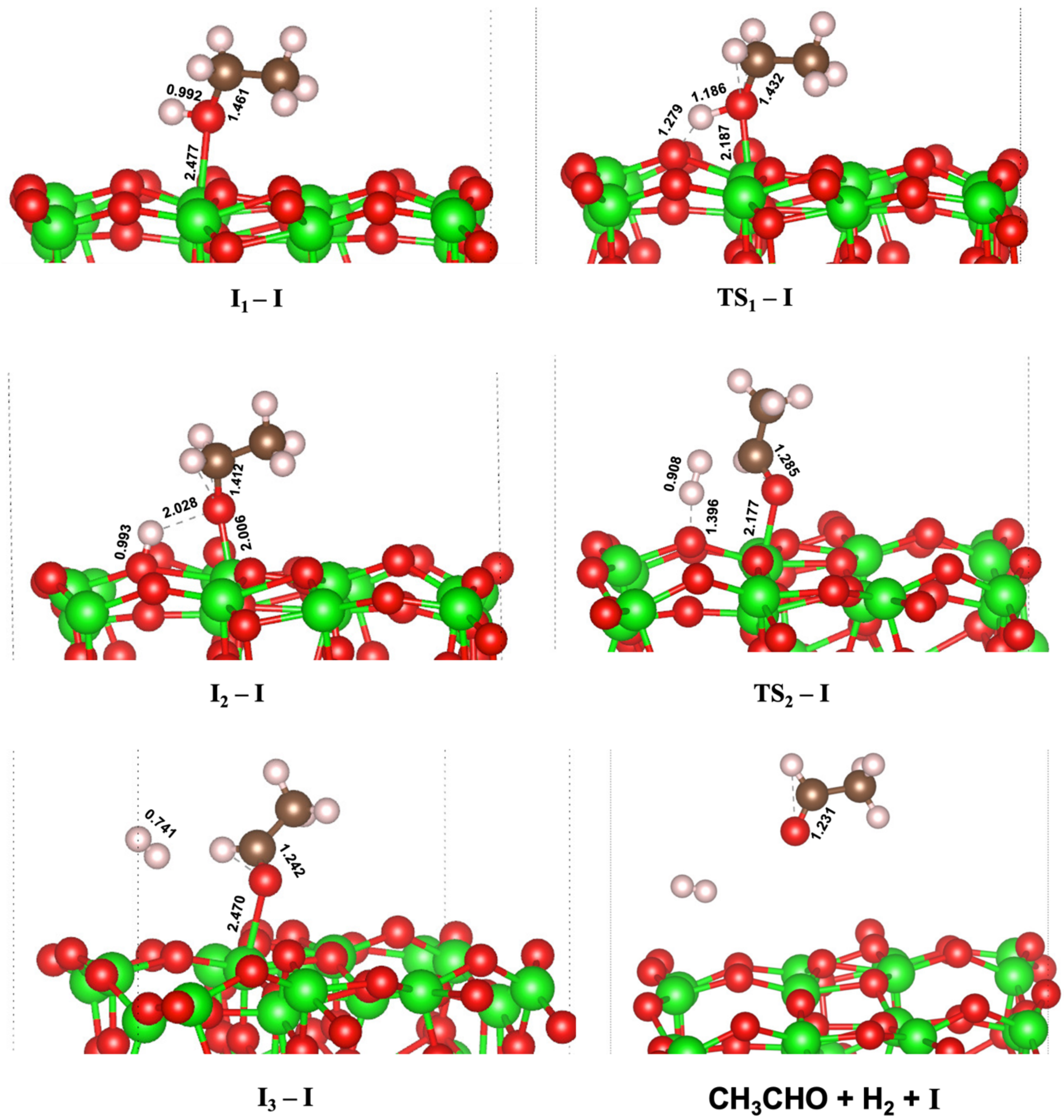

$I_1 - I$ **$TS_1 - I$**

$I_2 - I$ **$TS_2 - I$**

$I_3 - I$ **$CH_3CHO + H_2 + I$**

Figure 4. The structure of intermediates (I_1-**I**, I_2-**I**, I_3-**I**) and transition states (TS_1- **I**, TS_2- **I**), and products ($CH_3CHO + H_2$ + **I**) along the free energy profile for the dehydrogenation of CH_3CH_2OH to produce CH_3CHO and H_2 on the m-ZrO_2(111) surface.

Table 1. Values of free energy of reaction (ΔG_r), activation energy (ΔG_a), and rate constants for forward (K_{for}) and backward (K_{back}) reactions at 473.15K of the two steps corresponding to the dehydrogenation of CH_3CH_2OH to produce CH_3CHO and H_2 on the m-ZrO_2(111) surface.

	m-ZrO2(111) surface			
	ΔG_r (eV)	ΔG_a (eV)	$K_{for}(s^{-1})$	$K_{back}(s^{-1})$
I_1-I ⇋ I_2-I	-0.21	0.36	1.59×10^{9}	7.84×10^{6}
I_2-I ⇋ I_3-I	0.40	1.79	7.09×10^{-12}	1.37×10^{-2}

3.3.2 - CH_3CH_2OH Dehydrogenation Over Au_{13} Cluster

On the Au_{13} cluster, the I_1-**II** exhibits the interaction of O atom of CH_3CH_2OH with the Au atom with the lowest coordination number. The Au-$O_{Ethanol}$ bond length is 2.38 Å, and the adsorption energy of ΔG_r= -0.61 eV, similar to Silva *et al.*[84] reported. The charge transferred from CH_3CH_2OH to the Au_{13} cluster was 0.10 e. As expected, the more significant charge transfer indicates a strong covalent interaction between the adsorbed CH_3CH_2OH and Au_{13} cluster. In the first step, via transition state, TS_1-**II**, the cleavage of the O-H bond of CH_3CH_2OH is accompanied by the formation of an Au-H, Notably, a high energy barrier of ΔG_a=1.84 eV was calculated. In the intermediate I_2-**II**, the H atom interacts with two Au atoms to form a triangle. These results are in agreement with previous results reported on similar Au model systems[85]. Furthermore, the rate constant indicates that the backward reaction is ten orders of magnitude higher than the forward reaction, highlighting the unfavorable nature of the reaction.

In TS_2-**II**, as observed in the m-ZrO2(111) surface, the CH_3CH_2O moiety rotates to facilitate the interaction of H from the αC–H to the H bonded on the Au top site and the adjacent Au atom from the Au_{13} cluster. The Au-O bond length decreased by 0.284 Å, while the αC-O bond length increased by 0.178 Å.

Although the rate constant for H_2 formation from CH_3CH_2O over the Au_{13} cluster is approximately nine orders of magnitude lower than the backward reaction, the activation energy for this reaction is high, 1.42 eV. These values still indicate that H_2 formation is unlikely.

In intermediate I_3-**II**, H_2 is generated, and CH_3CHO moiety is adsorbed on the surface of the Au_{13} cluster. The αC-O bond length is reduced to 1.244 Å, and the Au-O bond length decreases by 0.078 Å, exhibiting a similar bond length and adsorption energy ΔG_r to that observed in I_1-**II**. Finally, the desorption energy of CH_3CHO, I_4-II, was determined to be ΔG_r= 0.52 eV on the Au_{13} cluster. The Au_{13} cluster was less effective for converting CH_3CH_2OH to CH_3CHO, it exhibited greater efficiency for H_2 formation compared to m-ZrO_2(111). However, this process still requires high energy, and the microkinetic modeling indicates unfavorable reaction rates for all reactions.

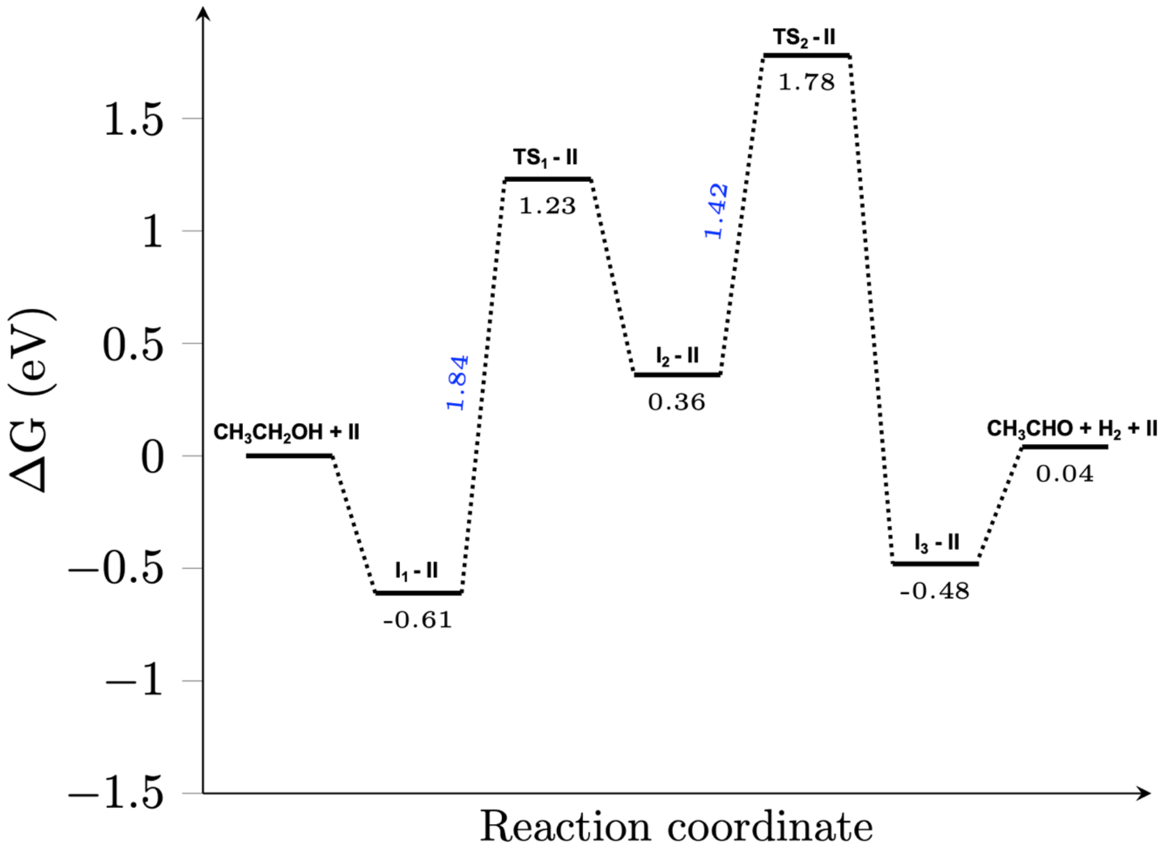

Figure 5. The calculated free energy profile of CH_3CH_2OH dehydrogenation on the Au_{13} cluster.

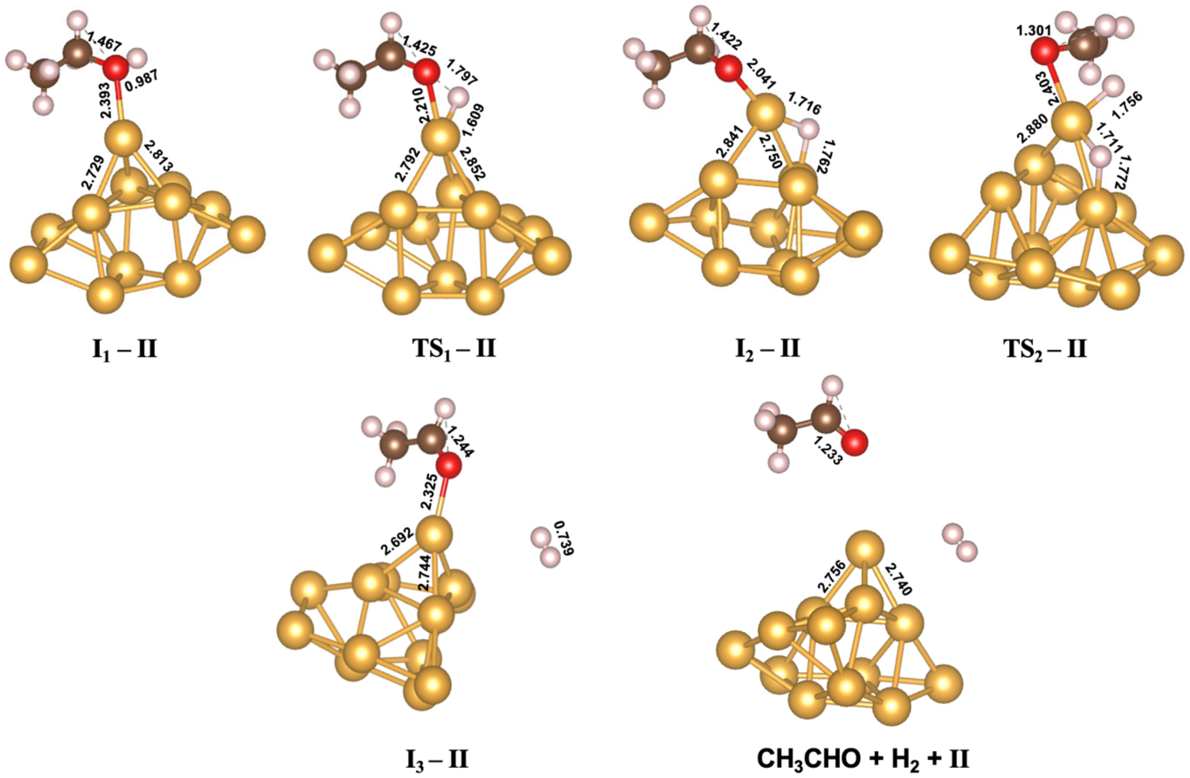

Figure 6. The structure of intermediates (I_1-**II**, I_2- **II**, I_3- **II**) and transition states (TS_1- **II**, TS_2-**II**), and products ($CH_3CHO + H_2 +$ **II**) along the free energy profile for the dehydrogenation of CH_3CH_2OH to produce CH_3CHO and H_2 on the Au_{13} cluster.

Table 2. Values of free energy of reaction (ΔG_r), activation energy (ΔG_a), and rate constants for forward (K_{for}) and backward (K_{back}) reactions at 473.15K of the two corresponding steps to the dehydrogenation of CH_3CH_2OH to produce CH_3CHO and H_2 on the Au_{13} cluster.

	Au_{13} cluster			
	ΔG_r (eV)	ΔG_a (eV)	$K_{for}(s^{-1})$	$K_{back}(s^{-1})$
I_1-II ⇋ I_2-II	0.97	1.84	2.51×10^{-7}	7.37×10^{3}
I_2-II ⇋ I_3-II	-0.84	1.42	6.37×10^{-3}	8.13×10^{-12}

3.3.3 - CH_3CH_2OH Dehydrogenation Over Au_{13} Cluster/m-ZrO_2(111) Surface

The adsorption of O atom of the O-H group of CH_3CH_2OH on the Zr site was selected based on its favorable adsorption and conversion characteristics for CH_3CH_2OH at this specific site observed in m-ZrO_2(111) surface. In the adsorption intermediate I_1-**III**, the Zr–O bond length is 2.467 Å with a ΔG_r of -0.91 eV. The charge transferred during this process is small, 0.02 e, comparable to that found on the m-ZrO_2(111) surface. As observed in the m-ZrO_2(111) surface, the first transition state, TS_1-**III**, is related to the cleavage of O-H in CH_3CH_2OH, with the assistance of the lattice oxygen to form the O-H bond. This reaction over the Au_{13} cluster/m-ZrO_2(111) surface must overcome a barrier height of ΔG_a=0.86 eV. It was observed that the rate constant of this reaction is three orders higher for the backward reaction than the forward reaction.

In the next step to generate H_2 over the Au_{13} cluster/m-ZrO_2(111) surface, the H atom bonded to the O surface must migrate towards the Au tom of the Au_{13} cluster closer to αC–H bond, introducing an additional stage in the reaction mechanism. This intermediate, I_2-**III**, has been observed experimentally.[86–90] This rearrangement has a barrier height of ΔG_a=0.54 eV, and the reaction is endothermic ΔG_r= 0.12 eV. As observed in the Au_{13} cluster, H is bonded to two adjacent Au atoms, with Au-H bond lengths of 1.697 and 1.884 Å. Although the rate constant of this reaction slightly favors the backward reaction, the reaction constant of the subsequent step is higher, suggesting that this stage is favored to proceed.

The transition state TS_3-**III** involves the breaking processes of both the Au-H bond and the αC–H bond of the CH_3CH_2O moiety with the concomitant formation of H_2.

Unlike the other catalysts, the CH_3CHO linked to the surface does not need to rotate. The required energy to generate H_2 was the lowest observed ΔG_a= 0.52 eV, and the thermodynamics of the reaction favors the process, as indicated by the exothermicity of ΔG_r= -0.48 eV. This was further confirmed by the rate constant of the reaction, where the forward reaction is six orders of magnitude higher than the backward reaction.

As observed on the m-ZrO_2(111) surface and Au_{13} cluster, after H_2 formation, in I_4-**III**, there is an increase in the Zr–O bond length by 0.458 Å, and in the CH_3CHO moiety, a decrease in the bond length of the αC–O by 0.161 Å.

At I_5-**III**, the desorption energy of CH_3CHO is ΔG_r= 0.57 eV, resembling the desorption value observed for the Au_{13} cluster, which is consistent with the findings of Bueno *et al.*, who reported a similar apparent experimental activation energy for the desorption of CH_3CHO from CH_3CH_2OH on Au/ZrO_2(111)[24].

Therefore, the kinetic and thermodynamic driving force for the favorable dehydrogenation of CH_3CH_2OH in this model system can be associated with the fact that the difference of energy among the TS of these three consecutive reaction steps, TS_1-**III**, TS_2-**III**, and TS_3-**III**, is low, i.e., 0.12 eV, and the large relative value of ΔG_r= -0.36 eV. These findings reveal that the Au_{13} cluster/m-ZrO_2(111) surface exhibits a favorable pathway for generating H_2 and CH_3CHO, suggesting fertile ground for further research. An analysis of the results shows that the TS_1-**III** presents the largest value of of ΔG_a, I_1-**III** → TS_1-**III**, 0.86 eV, while TS_3-**III** displays the higher relative free energy value along the profile, 0.07 eV. Therefore, following the work of Murdoch[91] the last stage, associated to the formation of H_2, can be considered the rate-limiting step for the dehydrogenation of CH_3CH_2OH

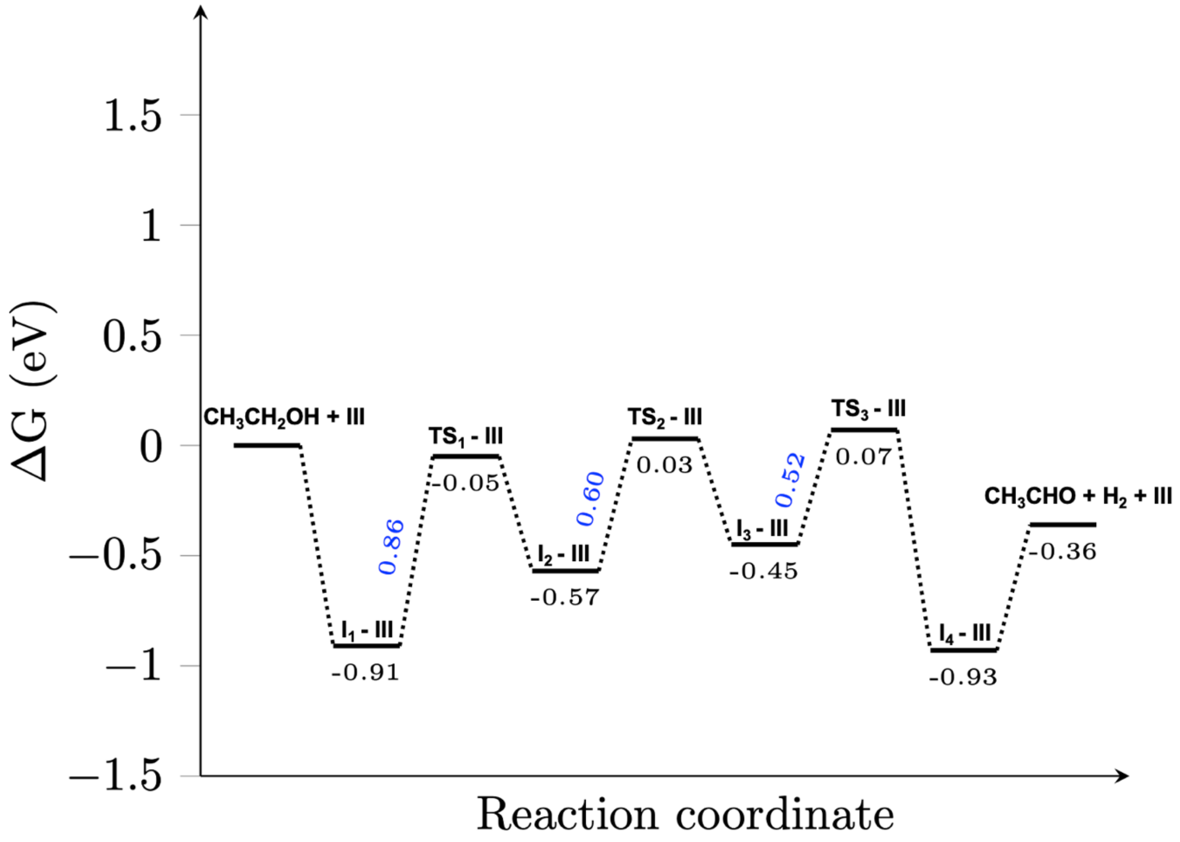

Figure 7. The calculated free energy profile of CH_3CH_2OH dehydrogenation on the Au_{13} cluster/m-ZrO_2(111).

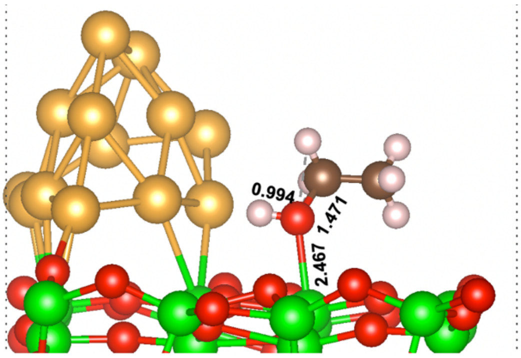

$I_1 – III$

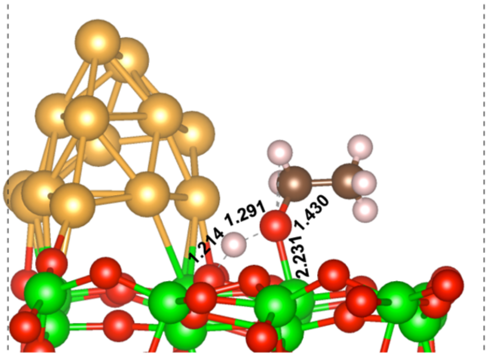

$TS_1 – III$

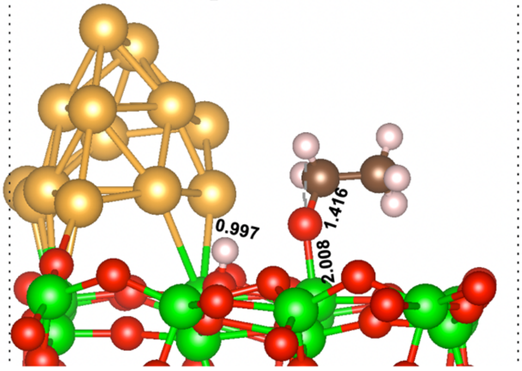

$I_2 – III$

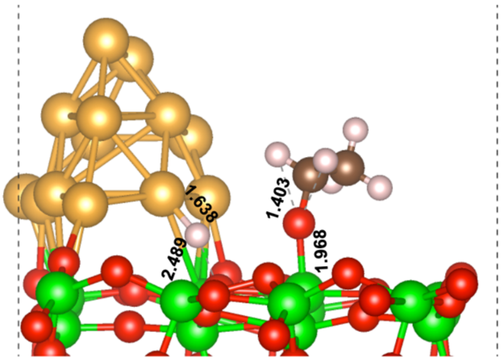

$TS_2 – III$

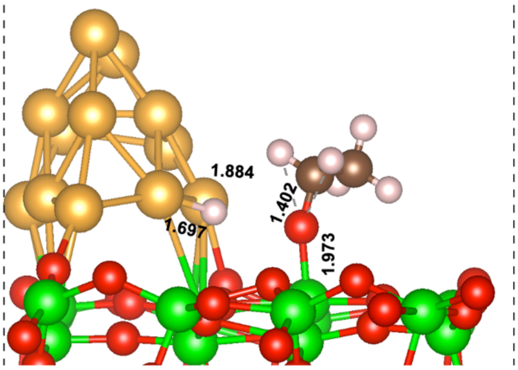

$I_3 – III$

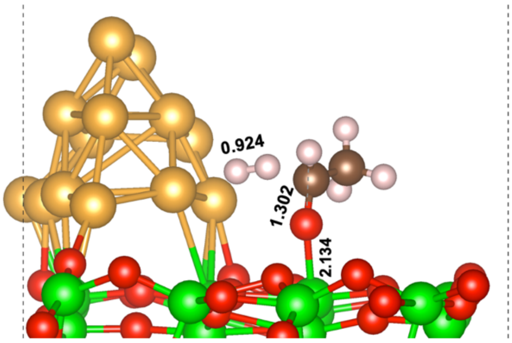

$TS_3 – III$

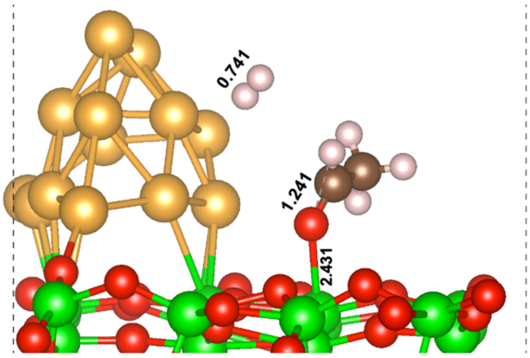

$I_4 – III$

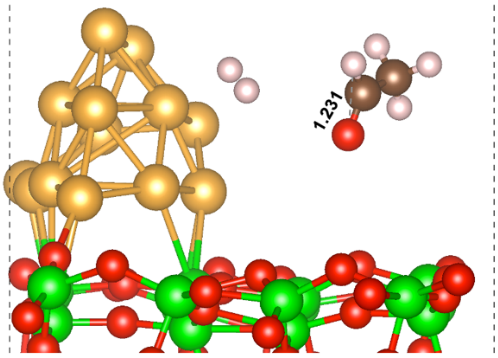

$CH_3CHO + H_2 + III$

Figure 8. The structure of intermediates (I_1-**III**, I_2- **III**, I_3- **III**) and transition states (TS_1- **III**, TS_2-**III**), and products (CH_3CHO + H_2 + **III**) along the free energy profile for the dehydrogenation of CH_3CH_2OH to produce CH_3CHO and H_2 on the Au_{13} cluster/m-ZrO_2(111) surface.

Table 3. Values of free energy of reaction (ΔG_r), activation energy (ΔG_a), and rate constants for forward (K_{for}) and backward (K_{back}) reactions at 473.15K of the three steps corresponding to the dehydrogenation reaction of CH_3CH_2OH to produce CH_3CHO and H_2 on the Au_{13} cluster/m-ZrO_2(111) surface.

	Au_{13} cluster/m-ZrO_2(111) surface			
	ΔG_r (eV)	ΔG_a (eV)	K_{for}(s^{-1})	K_{back}(s^{-1})
I_1-III ⇋ I_2-III	0.34	0.86	6.65×10^{3}	6.26×10^{6}
I_2-III ⇋ I_3-III	0.12	0.54	3.95×10^{6}	2.16×10^{7}
I_3-III ⇋ I_4-III	-0.48	0.52	6.23×10^{7}	3.68×10^{1}

3.4 - Conclusions

In our present study, we have calculated the free energy profiles for CH_3CH_2OH dehydrogenation to produce CH_3CHO and H_2 on models of the m-ZrO_2(111) surface, Au_{13} cluster, and Au_{13} cluster/m-ZrO_2(111) surface using DFT calculations and microkinetic model at 473.15K. On the m-ZrO_2(111) surface and Au13 cluster, dehydrogenation proceeds via two critical steps. The process begins with the cleavage of the O-H bond in CH_3CH_2OH, resulting in the formation of a CH_3CH_2O species. In the m-ZrO_2(111) surface, an O-H bond is generated with the lattice O atom, exhibiting lower activation energy and a higher rate constant, making this catalyst key in converting CH_3CH_2OH to CH_3CH_2O. In the Au_{13} cluster, this conversion occurs through the interaction of the H atom with the Au atom that has the lowest coordination number. The subsequent step corresponds to the formation of H_2 from the H atom absorbed on the surface with the H of the αC–H of the CH_3CH_2O moiety. Despite these pathways, microkinetic modeling indicates unfavorable reaction kinetics. In contrast, the Au_{13} cluster/m-ZrO_2(111) surface introduces an additional step, the H atom migrates from the surface to the Au_{13} cluster. Although the Au_{13} cluster/m-ZrO_2(111) surface requires this additional step, the energy barriers are lower. The corresponding TS of the three consecutive stages present similar relative energies. The negative free energies and reaction constants favor converting CH_3CH_2OH into CH_3CHO and H_2. These findings highlight the pivotal role of CH_3CH_2OH conversion to $CH3CH_2O$ species over the m-ZrO_2(111) surface and the Au_{13} cluster supported on m-ZrO_2(111) surface facilitates H_2 formation. This process demonstrates the potential of this catalytic system for an efficient and selective production of CH_3CHO and H_2, providing important insights into the design of advanced catalytic systems.

ACKNOWLEDGMENT

L.H.M. acknowledges supporting Coordenação de Aperfeiçoamento de Pessoal de Nível Superior - Brazil (CAPES) from grants PROEX process number 88887.500150/2020-00 and PRINT process number 88887.836086/2023-00. Acknowledges the National Laboratory for Scientific Computing (LNCC/ MCTI, Brazil) for providing HPC resources of the SDumont supercomputer, which have contributed to the research results reported within this work (URL: http://sdumont.lncc.br). A.L.C. acknowledges the Coordenação de

Aperfeiçoamento de Pessoal de Nível Superior - Brazil (CAPES): Finance Code 001 and from the Fundação de Amparo à Pesquisa de São Paulo - Brazil (FAPESP): number 2019/12501-0. J.A. acknowledges Universitat Jaume I (project UJI-B2022–56), Generalitat Valenciana (Conselleria de Innovación, Universidades, Ciencia y Sociedad Digital – project CIAICO/2021/122, and Ministerio de Ciencia e Innovación de España (project PID2022–141089NB-I00) for financially supporting this research.

CHAPTER 4

4 – Thesis Conclusions

This work explored the CH_3CH_2OH dehydrogenation and formation of CH_3CHO and H_2 over the m-ZrO_2(111) surface, Au_{13} cluster, and Au_{13} cluster/m-ZrO_2(111) surface using DFT. Thermodynamic and kinetic parameters were calculated at 473.15K, alongside the identification of transition states along the reaction mechanism. Additionally, microkinetic modeling allowed for determining rate constants throughout the reaction mechanism, providing comprehensive mechanistic insight into the catalytic process.

The proposed mechanism for the dehydrogenation of CH_3CH_2OH to CH_3CHO and H_2 on the m-ZrO_2(111) surface, the Au_{13} cluster, and the Au_{13} cluster/m-ZrO_2(111) surface. From the data obtained, it is indicated that m-ZrO_2(111) acts as a suitable catalyst for the conversion of CH_3CH_2OH to the intermediate CH_3CH_2O and H. However, in the subsequent step, the H_2 formation, m-ZrO_2(111), exhibits high activation energy and low rate constant associated with this reaction. The Au_{13} cluster exhibits high activation energy and a low rate constant for both reactions; however, its activation energy for H_2 formation is lower than that of m-ZrO_2(111), while its rate constant is higher. This indicates that the Au_{13} cluster is a more active catalyst for H_2 production than m-ZrO_2(111), highlighting its potential to enhance the efficiency of the dehydrogenation process. The Au_{13}/m-ZrO_2(111) surface exhibits an additional step involving the migration of the H atom from the m-ZrO_2(111) surface to the Au_{13} cluster. The transition states for the three consecutive stages exhibit similar relative energies. In contrast, the negative free energies and favorable rate constants indicate that the conversion of CH_3CH_2OH to CH_3CHO and H_2 is energetically favorable. Based on these results, m-ZrO_2(111) has been only demonstrated an efficient catalyst for the formation of the intermediate CH_3CH_2O and H atom from CH_3CH_2OH. Furthermore, the Au_{13} cluster supported on m-ZrO_2(111) exhibited effective and selective production of CH_3CHO and H_2 from CH_3CH_2OH. These findings provide valuable insights into the advanced design of catalytic systems.

CHAPTER 5

5 - References

(1) Errera, M. R.; Dias, T. A. da C.; Maya, D. M. Y.; Lora, E. E. S. Global Bioenergy Potentials Projections for 2050. *Biomass Bioenergy* **2023**, *170*, 106721.

(2) Pampararo, G.; Garbarino, G.; Comite, A.; Busca, G.; Riani, P. Acetaldehyde Production by Ethanol Dehydrogenation over Cu-ZnAl2O4: Effect of Catalyst Synthetic Strategies on Performances. *Chem Eng Sci* **2022**, *261*, 117937.

(3) Sun, J.; Wang, Y. Recent Advances in Catalytic Conversion of Ethanol to Chemicals. *ACS Catal* **2014**, *4* (4), 1078–1090.

(4) Eckert, M.; Fleischmann, G.; Jira, R.; Bolt, H. M.; Golka, K. Acetaldehyde. *Ullmann's Encyclopedia of Industrial Chemistry* **2006**, 191.

(5) Church, J. M.; Joshi, H. K. Acetaldehyde by Dehydrogenation of Ethyl Alcohol. *Ind Eng Chem* **1951**, *43* (8), 1804–1811.

(6) Pang, J.; Yin, M.; Wu, P.; Li, X.; Li, H.; Zheng, M.; Zhang, T. Advances in Catalytic Dehydrogenation of Ethanol to Acetaldehyde. *Green Chemistry* **2021**, *23* (20), 7902–7916.

(7) Choi, Y.; Wu, X.; Lee, J.; Na, K. Catalytic Dehydrogenation for Hydrogen Production Controlled by Metal-Supported Heterogeneous Catalysts. *Catal Sci Technol* **2024**.

(8) Iwasa, N.; Takezawa, N. Reforming of Ethanol. Dehydrogenation to Ethyl Acetate and Steam Reforming to Acetic Acid over Copper-Based Catalysts. *Bull Chem Soc Jpn* **1991**, *64* (9), 2619–2623.

(9) Shimokawabe, M.; Asakawa, H.; Takezawa, N. Characterization of Copper/Zirconia Catalysts Prepared by an Impregnation Method. *Appl Catal* **1990**, *59* (1), 45–58.

(10) Agrell, J.; Birgersson, H.; Boutonnet, M.; Melián-Cabrera, I.; Navarro, R. M.; Fierro, J. L. G. Production of Hydrogen from Methanol over Cu/ZnO Catalysts Promoted by ZrO2 and Al2O3. *J Catal* **2003**, *219* (2), 389–403.

(11) Jung, K. T.; Bell, A. T. Effects of Zirconia Phase on the Synthesis of Methanol over Zirconia-Supported Copper. *Catal Letters* **2002**, *80*, 63–68.

(12) Rhodes, M. D.; Bell, A. T. The Effects of Zirconia Morphology on Methanol Synthesis from CO and H2 over Cu/ZrO2 Catalysts: Part I. Steady-State Studies. *J Catal* **2005**, *233* (1), 198–209.

(13) Yang, Y.-L.; Fan, X.-L.; Liu, C.; Ran, R.-X. First Principles Study of Structural and Electronic Properties of Cubic Phase of ZrO2 and HfO2. *Physica B Condens Matter* **2014**, *434*, 7–13.

(14) Van Santen, R. A. Complementary Structure Sensitive and Insensitive Catalytic Relationships. *Acc Chem Res* **2009**, *42* (1), 57–66. https://doi.org/10.1021/ar800022m.

(15) Weng, B.; Lu, K. Q.; Tang, Z.; Chen, H. M.; Xu, Y. J. Stabilizing Ultrasmall Au Clusters for Enhanced Photoredox Catalysis. *Nat Commun* **2018**, *9* (1). https://doi.org/10.1038/s41467-018-04020-2.

(16) Chen, T.; Rodionov, V. O. Controllable Catalysis with Nanoparticles: Bimetallic Alloy Systems and Surface Adsorbates. *ACS Catalysis*. American Chemical Society June 3, 2016, pp 4025–4033. https://doi.org/10.1021/acscatal.6b00714.

(17) Astruc, D.; Lu, F.; Aranzaes, J. R. Nanoparticles as Recyclable Catalysts: The Frontier between Homogeneous and Heterogeneous Catalysis. *Angewandte Chemie - International Edition*. December 9, 2005, pp 7852–7872. https://doi.org/10.1002/anie.200500766.

(18) Stratakis, M.; Garcia, H. Catalysis by Supported Gold Nanoparticles: Beyond Aerobic Oxidative Processes. *Chemical Reviews*. August 8, 2012, pp 4469–4506. https://doi.org/10.1021/cr3000785.

(19) Qian, H.; Zhu, M.; Wu, Z.; Jin, R. Quantum Sized Gold Nanoclusters with Atomic Precision. *Acc Chem Res* **2012**, *45* (9), 1470–1479. https://doi.org/10.1021/ar200331z.

(20) Jin, R. Atomically Precise Metal Nanoclusters: Stable Sizes and Optical Properties. *Nanoscale*. Royal Society of Chemistry February 7, 2015, pp 1549–1565. https://doi.org/10.1039/c4nr05794e.

(21) Jin, R.; Zeng, C.; Zhou, M.; Chen, Y. Atomically Precise Colloidal Metal Nanoclusters and Nanoparticles: Fundamentals and Opportunities. *Chemical Reviews*. American Chemical Society September 28, 2016, pp 10346–10413. https://doi.org/10.1021/acs.chemrev.5b00703.

(22) Negishi, Y.; Kurashige, W.; Niihori, Y.; Nobusada, K. Toward the Creation of Stable, Functionalized Metal Clusters. *Physical Chemistry Chemical Physics*. November 21, 2013, pp 18736–18751. https://doi.org/10.1039/c3cp52837e.

(23) Wang, C.; Garbarino, G.; Allard, L. F.; Wilson, F.; Busca, G.; Flytzani-Stephanopoulos, M. Low-Temperature Dehydrogenation of Ethanol on Atomically Dispersed Gold Supported on ZnZrO x. *ACS Catal* **2016**, *6* (1), 210–218.

(24) Marcel R. Gallo, J.; de M. Augusto, T.; López-Castillo, A.; Ribeiro, M. C.; C.R. Rocha, T.; Osmari, T. A.; Lacerda, C. R.; Costa, M. S.; M.P. Marques, C.; Zanchet, D.; Ramirez, C. O.; Leite, E. R.; Maria C. Bueno, J. Fine-Tuning the Electronic Properties of Au toward Two-Dimensional Clusters with Higher Activity for Ethanol Conversion. *J Catal* **2024**, *432*. https://doi.org/10.1016/j.jcat.2024.115441.

(25) Born, M.; Heisenberg, W. Zur Quantentheorie Der Molekeln. *Original Scientific Papers Wissenschaftliche Originalarbeiten* **1985**, 216–246.

(26) Hohenberg, P.; Kohn, W. Inhomogeneous Electron Gas. *Physical review* **1964**, *136* (3B), B864.

(27) Louie, S. G.; Cohen, M. L. *Conceptual Foundations of Materials: A Standard Model for Ground-and Excited-State Properties*; Elsevier, 2006.

(28) Wellendorff, J.; Lundgaard, K. T.; Møgelhøj, A.; Petzold, V.; Landis, D. D.; Nørskov, J. K.; Bligaard, T.; Jacobsen, K. W. Density Functionals for Surface Science: Exchange-Correlation Model Development with Bayesian Error Estimation. *Phys Rev B Condens Matter Mater Phys* **2012**, *85* (23). https://doi.org/10.1103/PhysRevB.85.235149.

(29) Amsterdam Modeling Suite (AMS). *Nudged Elastic Band (NEB)*. https://www.scm.com/doc/AMS/Tasks/NEB.html (accessed 2024-09-30).

(30) Wu, Y.; Zhu, X.; Du, S.; Huang, G.; Zhou, B.; Lu, Y.; Li, Y.; Jiang, S. P.; Tao, L.; Wang, S. Promoted Hydrogen and Acetaldehyde Production from Alcohol Dehydrogenation Enabled by Electrochemical Hydrogen Pumps. *Proc Natl Acad Sci U S A* **2023**, *120* (27). https://doi.org/10.1073/pnas.2300625120.

(31) Preedavijitkul, S.; Autthanit, C.; Jadsadajerm, S.; Srijaroen, C.; Praserthdam, P.; Jongsomjit, B. Investigation on Deactivation of Cu-Cr Catalyst for Direct Ethanol Dehydrogenation to Ethyl Acetate, Acetaldehyde, and Hydrogen. *J Taiwan Inst Chem Eng* **2023**, *147*, 104895. https://doi.org/https://doi.org/10.1016/j.jtice.2023.104895.

(32) He, L.; Zhou, B.-C.; Sun, D.-H.; Li, W.-C.; Lv, W.-L.; Wang, J.; Liang, Y.-Q.; Lu, A.-H. Catalytic Conversion of Ethanol to Oxygen-Containing Value-Added Chemicals. *ACS Catal* **2023**, *13* (17), 11291–11304. https://doi.org/10.1021/acscatal.3c01481.

(33) Acetaldehyde Market by Process (Wacker Process, Oxidation of Ethanol, Dehydrogenation of Ethanol), Derivative (Pyridine & Pyridine Bases, Pentaerythritol), Application (Food & Beverage, Chemicals, Paints & Coatings), and Region - Global Forecast to 2022; 2018.

(34) Rising Use of Acetaldehyde in the Production of Various Organic Chemicals Sustain Market Growth. Global Industry Analysts, Inc. ; 2019.

(35) *ReportLinker Global Acetaldehyde Industry*; 2020.

(36) Ellis, W. B. Books: Ullmann's Encyclopedia of Industrial Chemistry. Wiley Online Library 1999.

(37) Jira, R. Acetaldehyde from Ethylene - A Retrospective on the Discovery of the Wacker Process. *Angewandte Chemie - International Edition*. November 16, 2009, pp 9034–9037. https://doi.org/10.1002/anie.200903992.

(38) Xia, W.; Wang, F.; Mu, X.; Chen, K. Remarkably Enhanced Selectivity for Conversion of Ethanol to Propylene over ZrO2 Catalysts. *Fuel Processing Technology* **2017**, *166*, 140–145. https://doi.org/10.1016/j.fuproc.2017.06.002.

(39) Pang, J.; Zheng, M.; He, L.; Li, L.; Pan, X.; Wang, A.; Wang, X.; Zhang, T. Upgrading Ethanol to N-Butanol over Highly Dispersed Ni–MgAlO Catalysts. *J Catal* **2016**, *344*, 184–193.

(40) Li, X.; Pang, J.; Wang, C.; Li, L.; Pan, X.; Zheng, M.; Zhang, T. Conversion of Ethanol to 1, 3-Butadiene over High-Performance Mg–ZrO x/MFI Nanosheet Catalysts via the Two-Step Method. *Green Chemistry* **2020**, *22* (9), 2852–2861.

(41) Sun, J.; Baylon, R. A. L.; Liu, C.; Mei, D.; Martin, K. J.; Venkitasubramanian, P.; Wang, Y. Key Roles of Lewis Acid–Base Pairs on Zn x Zr y O z in Direct Ethanol/Acetone to Isobutene Conversion. *J Am Chem Soc* **2016**, *138* (2), 507–517.

(42) Wang, Q.-N.; Weng, X.-F.; Zhou, B.-C.; Lv, S.-P.; Miao, S.; Zhang, D.; Han, Y.; Scott, S. L.; Schüth, F.; Lu, A.-H. Direct, Selective Production of Aromatic Alcohols from Ethanol Using a Tailored Bifunctional Cobalt–Hydroxyapatite Catalyst. *ACS Catal* **2019**, *9* (8), 7204–7216.

(43) Pang, J.; Yin, M.; Wu, P.; Li, X.; Li, H.; Zheng, M.; Zhang, T. Advances in Catalytic Dehydrogenation of Ethanol to Acetaldehyde. *Green Chemistry*. Royal Society of Chemistry October 21, 2021, pp 7902–7916. https://doi.org/10.1039/d1gc02799a.

(44) Xiang, H.; Xin, R.; Prasongthum, N.; Natewong, P.; Sooknoi, T.; Wang, J.; Reubroycharoen, P.; Fan, X. Catalytic Conversion of Bioethanol to Value-Added Chemicals and Fuels: A Review. *Resources Chemicals and Materials* **2022**, *1* (1), 47–68. https://doi.org/https://doi.org/10.1016/j.recm.2021.12.002.

(45) Dagle, R. A.; Winkelman, A. D.; Ramasamy, K. K.; Lebarbier Dagle, V.; Weber, R. S. Ethanol as a Renewable Building Block for Fuels and Chemicals. *Ind Eng Chem Res* **2020**, *59* (11), 4843–4853. https://doi.org/10.1021/acs.iecr.9b05729.

(46) Chitoria, A. K.; Mir, A.; Shah, M. A. A Review of ZrO2 Nanoparticles Applications and Recent Advancements. *Ceram Int* **2023**, *49* (20), 32343–32358. https://doi.org/https://doi.org/10.1016/j.ceramint.2023.06.296.

(47) Choudhary, V. R.; Dhar, A.; Jana, P.; Jha, R.; Uphade, B. S. A Green Process for Chlorine-Free Benzaldehyde from the Solvent-Free Oxidation of Benzyl Alcohol with Molecular Oxygen over a Supported Nano-Size Gold Catalyst. *Green Chemistry* **2005**, *7* (11), 768–770. https://doi.org/10.1039/b509003b.

(48) Bond, G. C.; Thompson, D. T. Catalysis by Gold. *Catalysis Reviews* **1999**, *41* (3–4), 319–388.

(49) Gong, J.; Mullins, C. B. Selective Oxidation of Ethanol to Acetaldehyde on Gold. *J Am Chem Soc* **2008**, *130* (49), 16458–16459.

(50) Gong, J.; Mullins, C. B. Surface Science Investigations of Oxidative Chemistry on Gold. *Acc Chem Res* **2009**, *42* (8), 1063–1073. https://doi.org/10.1021/ar8002706.

(51) Pina, C. Della; Falletta, E.; Rossi, M. Update on Selective Oxidation Using Gold. *Chem Soc Rev* **2012**, *41* (1), 350–369. https://doi.org/10.1039/c1cs15089h.

(52) Gombac, V.; Sordelli, L.; Montini, T.; Delgado, J. J.; Adamski, A.; Adami, G.; Cargnello, M.; Bernal, S.; Fornasiero, P. CuOx−TiO2 Photocatalysts for H2 Production from Ethanol and Glycerol Solutions. *J Phys Chem A* **2010**, *114* (11), 3916–3925. https://doi.org/10.1021/jp907242q.

(53) Montini, T.; Gombac, V.; Sordelli, L.; Delgado, J. J.; Chen, X.; Adami, G.; Fornasiero, P. Nanostructured Cu/TiO 2 Photocatalysts for H 2 Production from Ethanol and Glycerol Aqueous Solutions. *ChemCatChem* **2011**, *3* (3), 574–577. https://doi.org/10.1002/cctc.201000289.

(54) Biella, S.; Rossi, M. Gas Phase Oxidation of Alcohols to Aldehydes or Ketones Catalysed by Supported Gold. *Chemical communications* **2003**, No. 3, 378–379.

(55) Prati, L.; Rossi, M. Gold on Carbon as a New Catalyst for Selective Liquid Phase Oxidation of Diols. *J Catal* **1998**, *176* (2), 552–560.

(56) Sato, A. G.; Volanti, D. P.; Meira, D. M.; Damyanova, S.; Longo, E.; Bueno, J. M. C. Effect of the ZrO2 Phase on the Structure and Behavior of Supported Cu Catalysts for Ethanol Conversion. *J Catal* **2013**, *307*, 1–17. https://doi.org/10.1016/j.jcat.2013.06.022.

(57) Guan, Y.; Hensen, E. J. M. Ethanol Dehydrogenation by Gold Catalysts: The Effect of the Gold Particle Size and the Presence of Oxygen. *Appl Catal A Gen* **2009**, *361* (1–2), 49–56.

(58) Gazsi, A.; Koós, A.; Bánsági, T.; Solymosi, F. Adsorption and Decomposition of Ethanol on Supported Au Catalysts. *Catal Today* **2011**, *160* (1), 70–78. https://doi.org/10.1016/j.cattod.2010.05.007.

(59) Hernández-Ramírez, E.; Wang, J. A.; Chen, L. F.; Valenzuela, M. A.; Dalai, A. K. Partial Oxidation of Methanol Catalyzed with Au/TiO 2 , Au/ZrO 2 and Au/ZrO 2 -TiO 2 Catalysts. *Appl Surf Sci* **2017**, *399*, 77–85. https://doi.org/10.1016/j.apsusc.2016.12.068.

(60) Teo, B. K.; Sloane, N. J. A. *Magic Numbers in Polygonal and Polyhedral Clusters*; 1985; Vol. 24. https://pubs.acs.org/sharingguidelines.

(61) Chaves, A. S.; Piotrowski, M. J.; Da Silva, J. L. F. Evolution of the Structural, Energetic, and Electronic Properties of the 3d, 4d, and 5d Transition-Metal Clusters (30 TMn Systems for n = 2-15): A Density Functional Theory Investigation. *Physical Chemistry Chemical Physics* **2017**, *19* (23), 15484–15502. https://doi.org/10.1039/c7cp02240a.

(62) Gao, M.; Lyalin, A.; Takagi, M.; Maeda, S.; Taketsugu, T. Reactivity of Gold Clusters in the Regime of Structural Fluxionality. *Journal of Physical Chemistry C* **2015**, *119* (20), 11120–11130. https://doi.org/10.1021/jp511913t.

(63) Watanabe, Y. Atomically Precise Cluster Catalysis towards Quantum Controlled Catalysts. *Science and Technology of Advanced Materials*.

Institute of Physics Publishing December 1, 2014. https://doi.org/10.1088/1468-6996/15/6/063501.

(64) Heiz, U.; Bullock, E. L. Fundamental Aspects of Catalysis on Supported Metal Clusters. *J Mater Chem* **2004**, 564–577. https://doi.org/10.1039/b313560h.

(65) Giannozzi, P.; Baroni, S.; Bonini, N.; Calandra, M.; Car, R.; Cavazzoni, C.; Ceresoli, D.; Chiarotti, G. L.; Cococcioni, M.; Dabo, I. QUANTUM ESPRESSO: A Modular and Open-Source Software Project for Quantum Simulations of Materials. *Journal of physics: Condensed matter* **2009**, *21* (39), 395502.

(66) Blöchl, P. E. Projector Augmented-Wave Method. *Phys Rev B* **1994**, *50* (24), 17953.

(67) Wellendorff, J.; Lundgaard, K. T.; Møgelhøj, A.; Petzold, V.; Landis, D. D.; Nørskov, J. K.; Bligaard, T.; Jacobsen, K. W. Density Functionals for Surface Science: Exchange-Correlation Model Development with Bayesian Error Estimation. *Phys Rev B* **2012**, *85* (23), 235149.

(68) Delarmelina, M.; Quesne, M. G.; Catlow, C. R. A. Modelling the Bulk Properties of Ambient Pressure Polymorphs of Zirconia. *Physical Chemistry Chemical Physics* **2020**, *22* (12), 6660–6676.

(69) Li, J.; Meng, S.; Niu, J.; Lu, H. Electronic Structures and Optical Properties of Monoclinic ZrO 2 Studied by First-Principles Local Density Approximation+ U Approach. *Journal of Advanced Ceramics* **2017**, *6*, 43–49.

(70) Tolba, S. A.; Allam, N. K. Computational Design of Novel Hydrogen-Doped, Oxygen-Deficient Monoclinic Zirconia with Excellent Optical Absorption and Electronic Properties. *Sci Rep* **2019**, *9* (1), 10159.

(71) Lowther, J. E.; Dewhurst, J. K.; Leger, J. M.; Haines, J. Relative Stability of ZrO 2 and HfO 2 Structural Phases. *Phys Rev B* **1999**, *60* (21), 14485.

(72) Monkhorst, H. J.; Pack, J. D. Special Points for Brillouin-Zone Integrations. *Phys Rev B* **1976**, *13* (12), 5188–5192. https://doi.org/10.1103/PhysRevB.13.5188.

(73) Henkelman, G.; Uberuaga, B. P.; Jónsson, H. A Climbing Image Nudged Elastic Band Method for Finding Saddle Points and Minimum Energy Paths. *J Chem Phys* **2000**, *113* (22), 9901–9904.

(74) Smidstrup, S.; Pedersen, A.; Stokbro, K.; Jónsson, H. Improved Initial Guess for Minimum Energy Path Calculations. *J Chem Phys* **2014**, *140* (21).

(75) Bendavid, L. I.; Carter, E. A. CO2 Adsorption on Cu2O (111): A DFT+ U and DFT-D Study. *The Journal of Physical Chemistry C* **2013**, *117* (49), 26048–26059.

(76) Zhang, L.; Filot, I. A. W.; Su, Y.-Q.; Liu, J.-X.; Hensen, E. J. M. Transition Metal Doping of Pd (1 1 1) for the NO+ CO Reaction. *J Catal* **2018**, *363*, 154–163.

(77) Henkelman, G.; Arnaldsson, A.; Jónsson, H. A Fast and Robust Algorithm for Bader Decomposition of Charge Density. *Comput Mater Sci* **2006**, *36* (3), 354–360.

(78) Okumura, M.; Kitagawa, Y.; Haruta, M.; Yamaguchi, K. *DFT Studies of Interaction between O 2 and Au Clusters. The Role of Anionic Surface Au Atoms on Au Clusters for Catalyzed Oxygenation*. www.elsevier.com/locate/cplett.

(79) Valden, M.; Lai, X.; Goodman, D. Onset of Catalytic Activity of Gold Clusters on Titania with the Appearance of Nonmetallic Properties. *Science (1979)* **1998**, *281* (5383), 1647–1650.

(80) Fu, X.-P.; Guo, L.-W.; Wang, W.-W.; Ma, C.; Jia, C.-J.; Wu, K.; Si, R.; Sun, L.-D.; Yan, C.-H. Direct Identification of Active Surface Species for the Water–Gas Shift Reaction on a Gold–Ceria Catalyst. *J Am Chem Soc* **2019**, *141* (11), 4613–4623. https://doi.org/10.1021/jacs.8b09306.

(81) Puigdollers, A. R.; Pacchioni, G. CO Oxidation on Au Nanoparticles Supported on ZrO2: Role of Metal/Oxide Interface and Oxide Reducibility. *ChemCatChem* **2017**, *9* (6), 1119–1127. https://doi.org/10.1002/cctc.201601486.

(82) Yang, J.; Zheng, J.; Dun, C.; Falling, L. J.; Zheng, Q.; Chen, J.-L.; Zhang, M.; Jaegers, N. R.; Asokan, C.; Guo, J.; Salmeron, M.; Prendergast, D.; Urban, J. J.; Somorjai, G. A.; Guo, Y.; Su, J. Unveiling Highly Sensitive Active Site in Atomically Dispersed Gold Catalysts for Enhanced Ethanol Dehydrogenation. *Angewandte Chemie International Edition* **2024**. https://doi.org/10.1002/anie.202408894.

(83) Zhang, M.; Zhuang, J.; Yu, Y. A DFT Study on ZrO 2 Surface in the Process of Ethanol to 1,3-Butadiene: A Comprehensive Mechanism Elucidation. *Applied Surface Science*. Elsevier B.V. November 15, 2018, pp 1026–1034. https://doi.org/10.1016/j.apsusc.2018.07.115.

(84) Zibordi-Besse, L.; Tereshchuk, P.; Chaves, A. S.; Da Silva, J. L. F. Ethanol and Water Adsorption on Transition-Metal 13-Atom Clusters: A Density Functional Theory Investigation within van Der Waals Corrections. *J Phys Chem A* **2016**, *120* (24), 4231–4240. https://doi.org/10.1021/acs.jpca.6b03467.

(85) Boronat, M.; Corma, A.; Illas, F.; Radilla, J.; Ródenas, T.; Sabater, M. J. Mechanism of Selective Alcohol Oxidation to Aldehydes on Gold Catalysts: Influence of Surface Roughness on Reactivity. *J Catal* **2011**, *278* (1), 50–58. https://doi.org/10.1016/j.jcat.2010.11.013.

(86) Stobiński, L.; Zommer, L.; Duś, R. Molecular Hydrogen Interactions with Discontinuous and Continuous Thin Gold Films. *Appl Surf Sci* **1999**, *141* (3–4), 319–325.

(87) Stobiński, L.; Duś, R. Atomic Hydrogen Solubility in Thin Gold Films and Its Influence on Hydrogen Thermal Desorption Spectra from the Surface. *Appl Surf Sci* **1992**, *62* (1–2), 77–82.

(88) Stobiński, L.; Nowakowski, R.; Duś, R. Atomic Hydrogen Adsorption on Thin Discontinuous and Continuous Gold Films—Similarities and Differences. *Vacuum* **1997**, *48* (3–4), 203–207.

(89) Stobiński, L. Molecular and Atomic Deuterium Chemisorption on Thin Gold Films at 78 K: An Isotope Effect. *Appl Surf Sci* **1996**, *103* (4), 503–508.

(90) Conte, M.; Miyamura, H.; Kobayashi, S.; Chechik, V. Spin Trapping of Au-H Intermediate in the Alcohol Oxidation by Supported and Unsupported Gold Catalysts. *J Am Chem Soc* **2009**, *131* (20), 7189–7196. https://doi.org/10.1021/ja809883c.

(91) Murdoch, J. R. What Is the Rate-Limiting Step of a Multistep Reaction? *J Chem Educ* **1981**, *58* (1), 32.

Appendix A

Supplementary Information for “Unraveling the Mechanism of CH_3CH_2OH Dehydrogenation on m-ZrO_2(111) Surface, Au_{13} Cluster, and Au_{13}/m-ZrO_2(111) Surface: A DFT and Microkinetic Modeling Study”

SUPPORTING INFORMATION

Au_{13} cluster/m-ZrO_2(111) Structural

We conducted a comprehensive study of the interaction between the Au_{13} cluster and the m-ZrO_2(111) surface. Different positions were considered, and their corresponding energy values were compared, as detailed below.

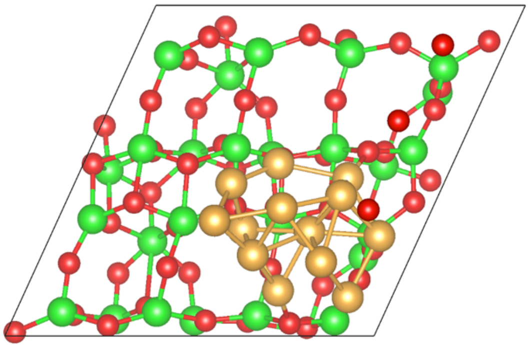

Position 1
E_{ads} = -4.33 eV

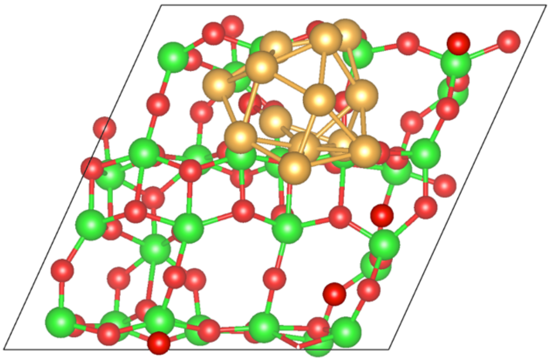

Position 2
E_{ads} = -4.23 eV

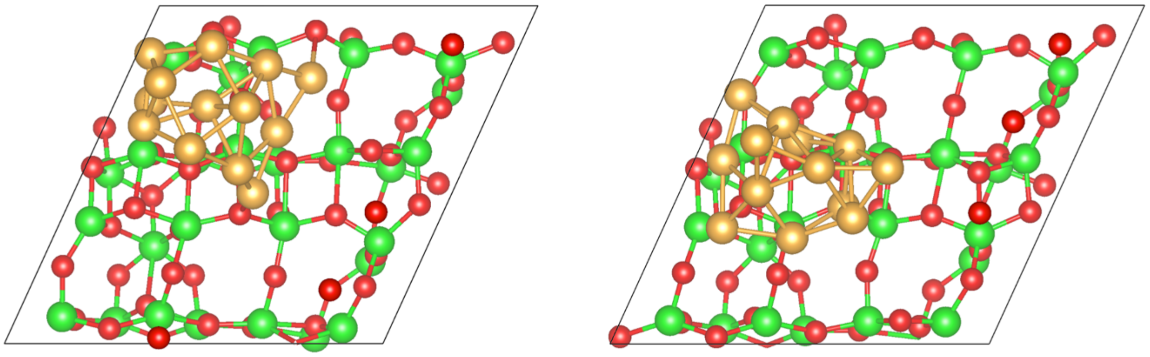

Position 3
E_{ads} = -3.88 eV

Position 4
E_{ads} = -3.81 eV

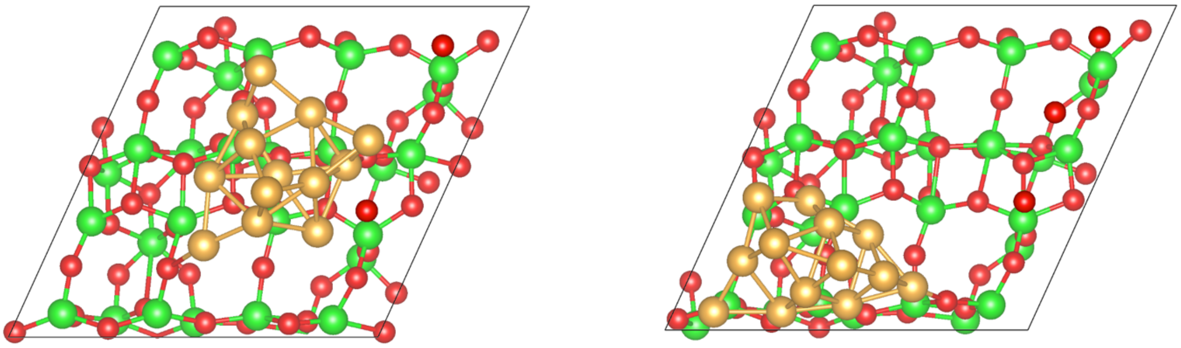

Position 5
E_{ads} = -4.63 eV

Position 6
E_{ads} = -4.89 eV

Figure S1. Positions of interaction between Au_{13} cluster on the surface of m-ZrO_2(111). Zr, O, and Au atoms are represented as green, red, and yellow spheres, respectively.

The configuration at position 6 was identified as the most stable among the possible interaction sites between the Au_{13} cluster and the m-ZrO_2(111) surface. Consequently, all subsequent calculations were conducted using this optimized system.

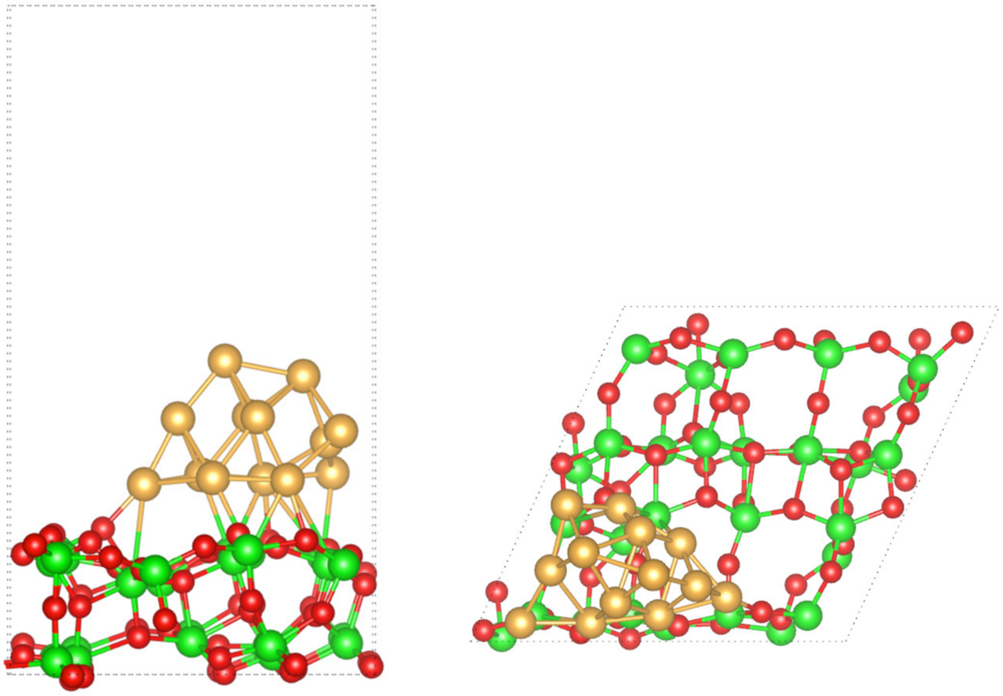

Side

Top view

Figure S3. Au_{13} cluster/m-ZrO_2(111). Zr, O, and Au atoms are represented as green, red, and yellow spheres, respectively.

Frequencies

To obtain Gibbs free energies, the zero-point energy (E_{ZPE}), entropy (S), and heat capacity (Cp) were added to quantum espresso energies. These contributions were obtained from the vibrational energies. Only frequencies higher than 200 cm^{-1} were considered to avoid unphysical entropic contributions. As E_{ZPE}, entropy, and heat capacity were computed by vibrational energies.

$$\Delta G = E_{DFT} + E_{ZPE} + \int_0^T C_p(T')dT' - T\Delta S$$

$$E_{ZPE} = \frac{1}{2} k_B \sum_i \epsilon_i$$

$$S = k_B \sum_i \left(\frac{\epsilon_i}{T\left(e^{\frac{\epsilon_i}{T}} - 1\right)} \right) - ln\left(1 - e^{\frac{-\epsilon_i}{T}}\right)$$

$$C_p = k_B \sum_i \left(\frac{x^2 e^x}{(e^x - 1)^2} \right); where\ x = \frac{\epsilon_i}{k_B T}$$

Transition states

The frequencies associated with CH_3CH_2OH dissociation correspond to the cleavage of the H atom from OH in ethanol and the formation of H in the catalyst surface. The frequencies associated with H_2 generation correspond to the cleavage of H from αC-H combined with the H surface bond.

Table S1. Characterization of the TS for CH_3CH_2OH dehydrogenation in m-ZrO_2(111).

Transition State	Barrier (eV)	Frequency (cm^{-1})
TS_1-I	0.36	1047.86i
TS_2-I	1.79	1094.38i

Table S2. Characterization of the TS for CH_3CH_2OH dehydrogenation in Au_{13}.

Transition State	Barrier (eV)	Frequency (cm^{-1})
TS_1 -II	1.84	632.05i
TS_2 -II	1.42	875.94i

Table S3. Characterization of the TS for CH_3CH_2OH dehydrogenation in Au_{13} cluster/m-ZrO_2(111).

Transition State	Barrier (eV)	Frequency (cm^{-1})
TS_1-III	0.86	1631.41i
TS_2-III	0.54	286.72i
TS_3-III	0.52	574.33i